universität wien

MASTERARBEIT / MASTER'S THESIS

Titel der Masterarbeit / Title of the Master's Thesis

Equilibrium conditions of multi-material particle distributions in SPH simulations of colliding planetesimals in early planetary systems

verfasst von / submitted by

Christoph Burger BSc BSc

angestrebter akademischer Grad / in partial fulfilment of the requirements for the degree of

Master of Science (MSc)

Wien, 2015 / Vienna 2015

Studienkennzahl lt. Studienblatt / degree programme code as it appears on the student record sheet:	A 066 861
Studienrichtung lt. Studienblatt / degree programme as it appears on the student record sheet:	Masterstudium Astronomie
Betreut von / Supervisor:	Univ. Prof. Dr. Rudolf Dvorak
Mitbetreut von / Co-Supervisor:	

Abstract

Providing the simulation algorithm with suitable initial conditions is a crucial first step in almost all numerical computations, except for the most trivial cases. Even the most sophisticated simulation program will not produce meaningful results if not started with an appropriate initial configuration, satisfying demands like isotropy, a low level of noise and physical accuracy. Some of these requirements are unique to *Smoothed Particle Hydrodynamics* (SPH) – the numerical method considered here – others are of fundamental relevance, independent of the chosen numerical technique.

The main focus of this thesis lies on considerations concerning initial conditions for subsequent SPH simulation runs. The geometrical arrangement of an initial SPH particle setup is discussed, particularly w.r.t. regular lattice configurations and associated symmetry effects. In order to avoid unphysical behavior the initial particle configuration has to be in a relaxed (i.e. equilibrated) state where necessary. This is of particular importance for simulations of giant collisions, where the involved bodies naturally exhibit a hydrostatic internal structure. Beyond the common numerical procedure, a *semi-analytical* approach for relaxation is introduced and validated, practically eliminating the need for spending significant amounts of valuable computing time solely for the production of a relaxed initial state in a lot of situations. Finally the basic relevance of relaxation itself is studied, focusing on collision simulations in different mass ranges important in the context of planet formation and the transport of water.

Zusammenfassung

Bei beinahe allen numerischen Simulationen – von den einfachsten Fällen abgesehen – stellt die Aufstellung geeigneter Anfangswerte einen entscheidenden ersten Schritt dar. Selbst das beste Simulationsprogramm wird ohne entsprechende Anfangskonfiguration keine sinnvollen Ergebnisse liefern, wobei Isotropie, geringes numerisches Rauschen, sowie physikalische Genauigkeit zentrale Voraussetzungen darstellen. Während manche Anforderungen eng an *Smoothed Particle Hydrodynamics* (SPH) – die hier verwendete numerische Methode – gekoppelt sind, können andere als relevant für alle numerischen Berechnungen betrachtet werden.

Das Hauptaugenmerk dieser Arbeit liegt auf Betrachtungen zu Anfangskonfigurationen für anschließende SPH-Simulationsläufe. Es werden geometrische Aspekte von anfänglichen SPH-Teilchenverteilungen diskutiert, insbesondere mit Blick auf Anordnungen in Form regelmäßiger Gitter und damit verbundener Symmetrieeffekte. Wo es die Problemstellung verlangt muss die Anfangskonfiguration in einem relaxierten Zustand (d.h. in einem Gleichgewicht) vorliegen, um unphysikalisches Verhalten zu unterbinden. Diese Anforderung ist besonders bei so genannten *giant collisions* von zentraler Bedeutung, bei denen die beteiligten Körper naturgemäß eine hydrostatische innere Struktur aufweisen. Jenseits der gebräuchlichen numerischen Relaxierung wird ein *semi-analytischer* Ansatz vorgestellt und validiert, der in vielen Fällen die Notwendigkeit beträchtliche Rechenzeit lediglich für die anfängliche Relaxierung aufzuwenden praktisch beseitigt. Abschließend wird die Bedeutung der Relaxierung an sich untersucht, wobei ein breiter Massenbereich an kollidierenden Körpern – wichtig im Kontext von Planetenentstehung und Wassertransport – betrachtet wird.

Contents

1 Introduction

During most of the time since the advent of modern science some centuries ago scientists followed a – at least conceptually – rather easy procedure, referred to as the *scientific method*. Even though it is hardly ever as simple as this suggests, the *classical* scientific method in brief is to formulate a hypothesis, construct practical predictions based on it and to test these predictions in appropriate experiments. The advent of powerful computers some decades ago however, made it possible to carry out experiments in a novel way, by conducting unprecedentedly large-scale numerical calculations, aiming to *simulate* the behavior of objects of the physical universe. Since even the best imaginable supercomputer can have only finite computing power (and accuracy), these machines will – in principle – never be able to reproduce the behavior of nature *exactly*, as it becomes immediately evident in chaotic systems for example[1]. However, in order to eventually obtain reliable results a suitable numerical model, incorporating (or rather approximating) all the physics which is important in the given context, has to be formulated, implemented, and – particularly important – tested against the outcome of real-life experiments. The whole subject of obtaining scientific results via numerical experiments becomes even more delicate when it is either impractical or even impossible to conduct such tests – in case they can neither be done in the laboratory nor is it possible to observe how nature *does them*. A good example are comet or asteroid impact events which cannot be carried out in laboratories once they exceed a certain magnitude, and occur only very rarely in nature. However, one popular exception in this case was the impact of *Shoemaker-Levy 9* on Jupiter in 1994, which was not only observed, but also extensively modelled, also with the aid of *Smoothed Particle Hydrodynamics* (SPH) by Asphaug and Benz (1996). What is generally summarized under the term *giant collisions* happens on an even larger scale, without any realistic chance to observe such an event in today's Solar System nor the possibility to do so in extrasolar planetary systems with current technology. Therefore numerical experiments are indeed *the only* possibility for obtaining detailed information on a collision's dynamics and its final outcome. This work deals with computer simulations particularly of these giant collision events by means of the SPH method, with a focus on the *art* of setting up proper initial conditions for these simulations, and their effect on the outcome.

Collisions, sometimes disruptive, sometimes not, are an ubiquitous process during all stages of planet formation. After planetesimals, the building blocks of the final planets, are formed, they continuously stick together to form ever larger bodies, which collide themselves to eventually form so-called *protoplanets* and – finally – planets. Therefore, in order to understand these processes in detail, it is evident to investigate individual collision outcomes. The current understanding of planet formation can be found comprehensively summarized e.g. by Morbidelli et al. (2012). One central question – closely related to planet formation – is the origin of the large amounts of water we find on Earth today. Addressing this issue is not only important for understanding the origin of Earth's water, but also to research on extrasolar planetary systems. As part of the

[1] On the other hand chaotic systems can be rather bad examples for pointing out the differences of real-life experiments and numerical ones, since they also depend critically on the precise experimental setup (e.g. in a lab), even though the processes during the experiment's runtime are carried out exactly (*by nature*), while numerical experiments always use a mere approximation thereof.

ongoing national science project *Pathways to Habitability*[2], possible processes for water delivery from the *wet* outer regions of a stellar system to its inner planets are investigated (see Dvorak et al. 2015b,c for more details). This is done on the one hand by running large-scale N-body simulations of protoplanetary disk evolution, where the initial conditions comprise a large number of planetesimals with varying water contents (see e.g. Bancelin et al., 2015). Individual (giant) collisions on the other hand are modelled by means of extensive SPH simulation campaigns, based on exactly the numerics presented in this thesis (see Maindl et al., 2014). A final goal is to eventually combine these two approaches by including SPH collision simulation outcomes into general N-body computations, in order to gain more conclusive insights into the late stages of planet formation in general, and the transport of water in particular.

Yet another open question in this context is the formation of the moon, with the so-called *giant impact hypothesis* being currently considered the most likely scenario thereof. After running N-body simulations to evaluate possible points of origin of the proposed Mars-sized impactor that hit the early Earth, Dvorak et al. (2015a) plan to further model this giant collision itself by performing detailed SPH computations, where the fate of possible water-reservoirs will be paid particular attention to.

This thesis is split into two main parts. In section 2 the basic principle of the SPH method is elaborated, before the equations and models governing solid-body mechanics (and hydrodynamics as a special case thereof) and their respective SPH representations are presented. Section 3 – the major part of the thesis – deals with the problem of setting up good initial conditions for a subsequent SPH simulation run. After discussing initial particle distributions mainly from a geometrical point of view in section 3.1, including numerical experiments on lattice symmetry effects, section 3.2 deals with the subject of *relaxation*, i.e. how to set up an initial particle distribution in a *self-consistent equilibrium state*. For this purpose a *semi-analytical* approach is introduced and validated against common numerical relaxation techniques. In addition the basic relevance of relaxation is studied with the masses of the colliding bodies as the main parameter.

[2]See *http://path.univie.ac.at/* for more details.

2 Smoothed Particle Hydrodynamics for continuum mechanics

Smoothed Particle Hydrodynamics (SPH) is a *mesh-free Lagrangian particle method*. In contrast to typical grid-based schemes SPH is based on freely interacting particles which represent the simulated system and carry the physical properties of their spatial region. The particles' motion is governed by the Lagrangian form of the equations of motion. While conventional grid-based schemes treat spatial derivatives via finite differences of adjacent grid cells, SPH is based on kernel interpolation of physical quantities. The basic idea behind it is to transform the partial differential equations (PDEs) arising from solid- and hydrodynamics into (an approximate system of) ordinary differential equations (ODEs). These equations can then in principle be solved by means of any method for solving ODEs that comes to mind.

The method was originally developed by Lucy (1977) and Gingold and Monaghan (1977) for simulating hydrodynamical problems in astrophysics. It was later extended by Libersky and Petschek (1991) to include solid-body physics. To date SPH has been applied to a large variety of fields, ranging from all kinds of astrophysical problems, over material science and high-velocity impacts, as far as computer-generated imagery[3]. A comprehensive review of the SPH method can be found e.g. in Monaghan (2005), Monaghan (1992) and in Schäfer (2005) – who focuses particularly on the treatment of solid-bodies. The details in the following representation are based mainly on the latter two works, unless stated otherwise.

SPH is said to be *easy, robust and fast*. Being independent of any kind of underlying grid eases the implementation of irregular shapes and free boundaries, and the particle nature of the method makes it particularly easy to include self-gravity. However, compared to grid-based schemes the local accuracy and the spatial resolution are typically lower. Therefore, depending on the specific situation, large particle numbers might be required to overcome these drawbacks.

In the following the basic principle of SPH is elaborated, before the SPH representations of the equations governing solid- and hydrodynamics are presented. All simulation results in this thesis are based on the SPH code developed by Schäfer (2005) (for a brief introduction see also Maindl et al., 2013) and using the full solid-body treatment as presented in the following sections. For modeling hydrodynamics alone, the respective expressions in sections 2.3, 2.4 and 2.5 along with an equation of state (section 2.6) would be sufficient.

2.1 SPH basic principle

The foundation of the SPH method lies within the approximation/smoothing of quantities $f(\vec{x})$ via the *Kernel function* $W(r,h)$, which is basically a spherically symmetric function in the radial coordinate r, that falls of rapidly enough towards larger r-values. The so-called *smoothing length* h determines its extension, i.e. its range of influence (more details on the Kernel function are provided in section 2.2). This approximation

$$f(\vec{x}) \quad \longrightarrow \quad \int f(\vec{x}')\, W\left(|\vec{x}-\vec{x}'|, h\right)\, dV' \qquad \left(= f(\vec{x}) + \mathcal{O}(h^2)\right) \tag{1}$$

[3] If you are interested in more examples of SPH applications in various fields visit the website http://www.nextlimit.com/ for example.

can also be considered a weighted average of the $f(\vec{x}')$, where the weights ($W(\dots)$) decrease with increasing distance $|\vec{x} - \vec{x}'|$ and $dV' = dx'dy'dz'$. This approximation is typically first-order accurate, with the error growing with h like $\mathcal{O}(h^2)$. It becomes exact for $h \to 0$, where the Kernel function tends to $\delta(\vec{x}' - \vec{x})$. The approximation in (1) can be extended to conveniently handle derivatives of the function $f(\vec{x})$, by using

$$\nabla_x f(\vec{x}) \quad \longrightarrow \quad \int f(\vec{x}')\, \nabla_x W\left(|\vec{x} - \vec{x}'|, h\right)\, dV' \quad . \tag{2}$$

This implies that derivatives act only on the Kernel function within the approximation, which is usually chosen to be (analytically) differentiable. In order to obtain a useful expression within a numerical scheme the integration has to be discretized. This leads to the following approximation of derivatives by means of a SPH-sum over all neighbouring particles[4]:

$$\nabla f(\vec{x}_i) \cong \sum_j \frac{m_j}{\rho_j}\, f(\vec{x}_j)\, \nabla_x W\left(|\vec{x}_i - \vec{x}_j|, h\right) \tag{3}$$

The i's and j's denote the considered SPH particles, where the expression calculates the gradient of the quantity f at position $\vec{x}_i$ by summing up over all neigbouring particles with indices j (at positions $\vec{x}_j$). The volume element in (2) was replaced by m_j/ρ_j, representing the volume assigned to particle j.

This approximation of partial (spatial-) derivatives finally makes it possible to convert the PDEs arising from solid -and hydrodynamics into ODEs, where all spatial derivatives have been replaced by SPH-sums (including only Kernel-derivatives anymore, which can usually be computed analytically). The individual treatment of the equations of solid- and hydrodynamics however, varies, and is summarized in the subsequent sections.

2.2 The Kernel function

One of the major ingredients for a successful SPH simulation is the choice of the right kernel function and a proper smoothing length. In practice the Kernel function $W(r, h)$ is chosen to be a spherically symmetric function which fulfills

$$\int W(r, h)\, dV = 1 \tag{4}$$

and

$$\lim_{h \to 0} W(r, h) = \delta(|\vec{x}|) \quad . \tag{5}$$

Particularly during the dawn of the SPH method Gaussians were sometimes used, like already (in three dimensions) by Gingold and Monaghan (1977):

$$W(r, h) = \left(\frac{1}{\pi\, h^2}\right)^{\frac{3}{2}} \exp\left(-\frac{r^2}{h^2}\right) \quad . \tag{6}$$

The main problem with this choice is that it is non-vanishing for the whole space, resulting in each particle interacting always with *all* other particles constituting the simulation.

[4] *Neigbouring particles* – or *interaction partners* – are all SPH particles that are located within the range of the Kernel function w.r.t. the particle under consideration. For particles located outside, the Kernel function has already dropped to zero.

This finally leads to an N^2 algorithm, where N is the overall particle number. In order to overcome these obstacles a Kernel function with compact support may be more convenient, and allows for including only neighbours within a certain range to a particle's SPH-sums. A widely used Kernel of that kind is based on a cubic B-spline function and was introduced by Monaghan and Lattanzio (1985). The precise formulation (in three dimensions), used in all simulations throughout this thesis, is given in Schäfer (2005):

$$W(r,h) = \frac{8}{\pi\, h^3} \begin{cases} 6\,(r/h)^3 - 6\,(r/h)^2 + 1 & 0 \le r/h < 1/2 \\ 2\,(1 - r/h)^3 & 1/2 \le r/h \le 1 \\ 0 & r/h > 1 \end{cases} . \tag{7}$$

Its first derivative (gradient) – necessary for evaluating SPH-sums – is then given by:

$$\frac{\partial W(r,h)}{\partial r} = \frac{48}{\pi\, h^4} \begin{cases} 3\,(r/h)^2 - 2\,(r/h) & 0 \le r/h < 1/2 \\ -(1 - r/h)^2 & 1/2 \le r/h \le 1 \\ 0 & r/h > 1 \end{cases} . \tag{8}$$

Both functions (7) and (8) (more precisely their radial components) are plotted together in *Fig. 1*.

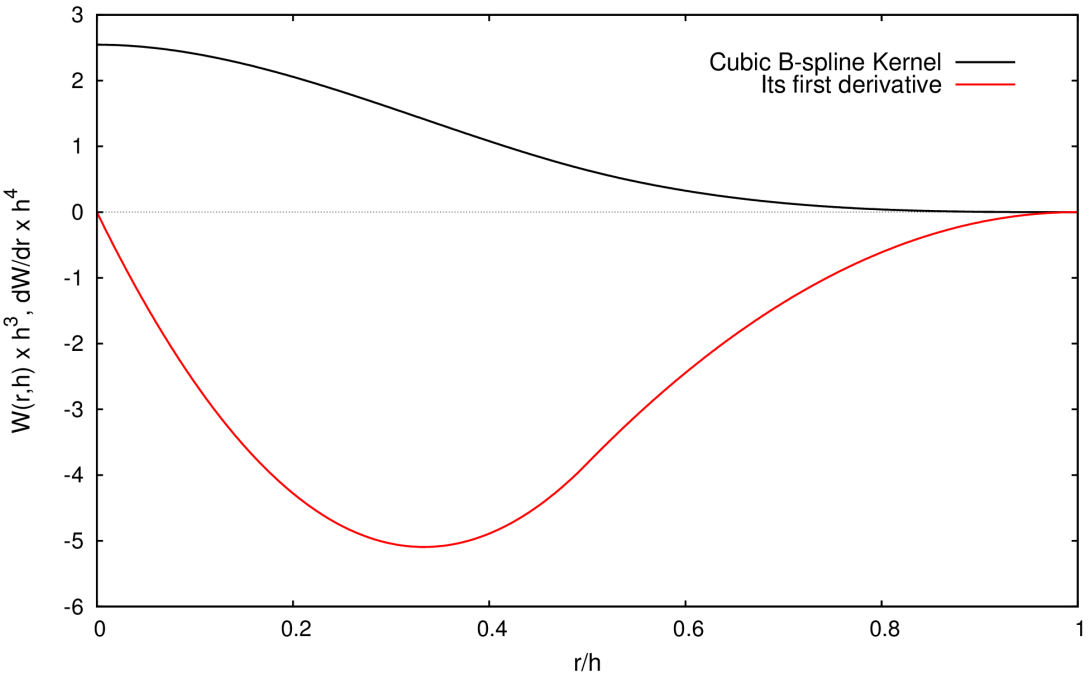

Figure 1 The cubic B-spline Kernel (7) used throughout this thesis in black, and its first derivative (8) in red.

The smoothing length h determines the Kernel's size and therefore the number of interaction partners. In principle it can be chosen either fixed (in space *and* time) or

variable, e.g. determined via an always fixed number of interaction partners. More details on variable smoothing lengths are provided for example by Schäfer (2005), while for the simulations presented in this thesis a fixed smoothing length is used, chosen to be slightly larger than 2 times the mean distance between particles in the initial configuration – which is always (at least close to) a regular lattice.

2.3 Conservation of mass – The continuity equation

The conservation of mass in either a fluid or a solid body is represented by the continuity equation, which reads

$$\frac{\partial \rho}{\partial t} + \frac{\partial (\rho\, v_\alpha)}{\partial x_\alpha} = 0 \tag{9}$$

(where $\rho\vec{v}$ is the flux density), or in Lagrangian form[5], which is important in the context of SPH:

$$\frac{d\rho}{dt} + \rho \frac{\partial v_\alpha}{\partial x_\alpha} = 0 \quad . \tag{10}$$

Here and in the following the Einstein summation convention is used whenever applicable, in a form implying summation over all indices that appear twice in a single term. As for most other physical equations various SPH representations of (10) exist. In most pure hydrodynamics simulations the continuity equation is not integrated, but a discretized version of (1) is used directly:

$$\rho_i = \sum_j m_j W_{ij} \quad . \tag{11}$$

Here and in the following the shortened notation $f_i = f(\vec{x}_i)$ and $W_{ij} = W\left(|\vec{x}_i - \vec{x}_j|, h\right)$ is used whenever applicable. However, particularly when simulating solid bodies this can result in problems at material boundaries, especially at the bodies' outer boundaries. Since particles at (or close to) the boundary of a solid body have in general less interaction partners than particles located well inside it, applying (11) might result in lower density values, even for an in principle homogeneous body. One consequence thereof would be physically wrong pressure values (via the applied equation of state, cf. section 2.6), likely resulting in unstable material boundaries. A straight-forward and commonly used solution is to simply integrate the continuity equation, instead of obtaining density values merely via (11). Starting with some initial density distribution, changes occur only when particles move relative to each other. A possible SPH representation for integrating the continuity equation is given by

$$\frac{d\rho_i}{dt} = -\sum_j m_j (\vec{v}_j - \vec{v}_i) \cdot \nabla_i W_{ij} \quad . \tag{12}$$

[5] In this form the time derivative is a total/substantial one. From a mathematical point of view the partial and total time derivative are simply connected by the chain rule, e.g. for the density $\rho = \rho(\vec{x}(t), t)$ via $d\rho/dt = \partial\rho/\partial t + (\vec{v} \cdot \nabla)\rho$. From a physical point of view the total time derivative consists of a local part (here $\partial\rho/\partial t$), giving the temporal change at a fixed location, and a convective one (here $(\vec{v} \cdot \nabla)\rho$), providing the considered quantity's change caused by movement to a different location (where the quantity has in general a different value). Thus the total time derivative gives a quantity's change as seen by an observer moving with the flow, i.e. moving in the flow's velocity field $\vec{v}$.

An alternative representation, in use for solid body simulations (Randles and Libersky, 1996), is obtained by starting with the continuity equation in a form that is the direct result of applying (3) to (10)

$$\frac{d\rho_i}{dt} = -\rho_i \sum_j \frac{m_j}{\rho_j} \vec{v}_j \cdot \nabla_i W_{ij} + \rho_i \vec{v}_i \cdot \nabla 1 \quad , \tag{13}$$

where an additional zero term $(\rho_i \vec{v}_i \cdot \nabla 1)$ has been added. Replacing $\nabla 1$ by $\sum_j \frac{m_j}{\rho_j} \nabla_i W_{ij}$ (which is just the SPH-sum (3) for a constant $f(\vec{x}_i) = 1$) and combining the two sums one finally ends up with

$$\frac{d\rho_i}{dt} = -\rho_i \sum_j \frac{m_j}{\rho_j} (\vec{v}_j - \vec{v}_i) \cdot \nabla_i W_{ij} \quad . \tag{14}$$

This is also the representation of the continuity equation that has been used for all computations presented in this thesis.

2.4 Conservation of momentum – The equation of motion

An equation of motion describes the acceleration of a certain part of the fluid or the solid body by evaluating (the sum of) all forces acting on it. To demonstrate this exemplarily, an ideal (non-viscous) fluid under the influence of a gravitational field is considered. Each mass element dm of that fluid is subject to forces due to gravity $\vec{F}_g = \vec{g}\, dm$ and a pressure gradient $\vec{F}_p = -\nabla p\, dV$, with the gravitational acceleration $\vec{g}$ and $dm = \rho\, dV$. Combining this one ends up with

$$\begin{aligned} dm \frac{d\vec{v}}{dt} &= \vec{F}_g + \vec{F}_p \\ dm \frac{d\vec{v}}{dt} &= \vec{g}\, dm - \nabla p \frac{dm}{\rho} \\ \frac{d\vec{v}}{dt} &= \vec{g} - \frac{1}{\rho} \nabla p \quad , \end{aligned} \tag{15}$$

which is the equation of motion for an ideal fluid, usually denoted *Euler equation*, in its Lagrangian form (cf. section 2.3). The substantial derivative for $\vec{v} = \vec{v}(\vec{x}(t), t)$ on the left-hand side describes the change in velocity for a comoving observer, and arises quite naturally from the fact that this derivation directly follows a mass element (and the forces acting on it), and thus *moves with the flow*. Changing to the SPH picture, the mass elements can be thought of as being replaced by SPH particles.

In the more general case, when considering elastic deformations of solid bodies, the simple pressure gradient has to be replaced by the divergence of the stress tensor $\sigma_{\alpha\beta}$, providing the force acting at a certain location inside the body, caused by internal stresses. Solid body characteristics beyond that, namely plasticity and brittle failure, are treated in section 2.7. The equation of motion in the elastic case (without gravitational influence) can be written as

$$\frac{dv_\alpha}{dt} = \frac{1}{\rho} \frac{\partial \sigma_{\alpha\beta}}{\partial x_\beta} \quad , \tag{16}$$

where the stress tensor can be split up into a pressure part and the deviatoric stress tensor $S_{\alpha\beta}$ ($\delta_{\alpha\beta}$ denotes the Kronecker delta):

$$\sigma_{\alpha\beta} = -p\,\delta_{\alpha\beta} + S_{\alpha\beta} \quad . \tag{17}$$

For vanishing shear stresses, e.g. during mere compression, the stress tensor reduces to its pressure part $\sigma_{\alpha\beta} = -p\,\delta_{\alpha\beta}$, and the right-hand side of (16) is reduced to the pressure term in (15). In contrast to pure hydrodynamics (16) is not sufficient to entirely describe the elastic behavior of a solid body, since the evolution of $S_{\alpha\beta}$ is not specified. Some further phenomenological equations, so-called *constitutive equations*[6] are required. In the elastic regime this is simply *Hooke's law*, describing a linear relation between internal stresses and strains. Based on the three-dimensional extension thereof, the time evolution of the deviatoric stress tensor can be expressed as

$$\frac{dS_{\alpha\beta}}{dt} = 2\mu\left(\dot{\epsilon}_{\alpha\beta} - \frac{1}{3}\delta_{\alpha\beta}\dot{\epsilon}_{\gamma\gamma}\right) + S_{\alpha\gamma}R_{\gamma\beta} + S_{\beta\gamma}R_{\gamma\alpha} \quad , \tag{18}$$

with the (material-dependent) shear modulus μ and the strain rate tensor $\dot{\epsilon}_{\alpha\beta}$, given by

$$\dot{\epsilon}_{\alpha\beta} = \frac{1}{2}\left(\frac{\partial v_\alpha}{\partial x_\beta} + \frac{\partial v_\beta}{\partial x_\alpha}\right) \quad . \tag{19}$$

The rotation rate tensor $R_{\alpha\beta}$, required for ensuring independence of the material's frame of reference, can be expressed as

$$R_{\alpha\beta} = \frac{1}{2}\left(\frac{\partial v_\alpha}{\partial x_\beta} - \frac{\partial v_\beta}{\partial x_\alpha}\right) \quad , \tag{20}$$

where this specific implementation is called the *Jaumann rate form*. Here the underlying physics and the equations' SPH representations shall be only briefly summarized, while for a more detailed description the reader is referred to Schäfer (2005). Since a straightforward SPH representation of the Euler equation (15) (excluding gravity) lacks linear and angular momentum conservation in practice, a symmetrized formula can be obtained by using the identity

$$\frac{\nabla p}{\rho} = \nabla\left(\frac{p}{\rho}\right) + \frac{p}{\rho^2}\nabla\rho \quad , \tag{21}$$

resulting in

$$\frac{d\vec{v}_i}{dt} = -\sum_j m_j\left(\frac{p_i}{\rho_i^2} + \frac{p_j}{\rho_j^2}\right)\nabla_i W_{ij} \quad . \tag{22}$$

A common alternative formulation is given by

$$\frac{d\vec{v}_i}{dt} = -\sum_j m_j\frac{p_i + p_j}{\rho_i\,\rho_j}\nabla_i W_{ij} \quad . \tag{23}$$

[6] In general a consitutive equation can be defined as a relation between physical quantities that is not a fundamental physical law, but rather often of phenomenological origin, being valid in some situations/materials, but perhaps failing in others. Another famous constitutive equation – besides Hooke's law – is Ohm's law.

Proceeding to solid body dynamics, i.e. the elastic regime theoretically described above, two possibilities of the equation of motion's (16) SPH representation are

$$\frac{d(v_i)_\alpha}{dt} = \sum_j m_j \left(\frac{(\sigma_i)_{\alpha\beta}}{\rho_i^2} + \frac{(\sigma_j)_{\alpha\beta}}{\rho_j^2} \right) \frac{\partial W_{ij}}{\partial x_\beta} \tag{24}$$

and

$$\frac{d(v_i)_\alpha}{dt} = \sum_j m_j \frac{(\sigma_i)_{\alpha\beta} + (\sigma_j)_{\alpha\beta}}{\rho_i \rho_j} \frac{\partial W_{ij}}{\partial x_\beta} \quad , \tag{25}$$

where the stress tensor can be computed as the sum of a pressure term and the deviatoric stress tensor $S_{\alpha\beta}$ as given in (17). In order to obtain the time evolution of $S_{\alpha\beta}$, given in (18), SPH representations of the strain rate tensor $\dot{\epsilon}_{\alpha\beta}$ (19) and the rotation rate tensor $R_{\alpha\beta}$ (20) are required. Again alternative representations exist, for the strain rate tensor

$$(\dot{\epsilon}_i)_{\alpha\beta} = \frac{1}{2} \sum_j \frac{m_j}{\rho_j} \left([(v_j)_\alpha - (v_i)_\alpha] \frac{\partial W_{ij}}{\partial (x_i)_\beta} + [(v_j)_\beta - (v_i)_\beta] \frac{\partial W_{ij}}{\partial (x_i)_\alpha} \right) \tag{26}$$

or

$$(\dot{\epsilon}_i)_{\alpha\beta} = \frac{1}{2} \frac{1}{\rho_i} \sum_j m_j \left([(v_j)_\alpha - (v_i)_\alpha] \frac{\partial W_{ij}}{\partial (x_i)_\beta} + [(v_j)_\beta - (v_i)_\beta] \frac{\partial W_{ij}}{\partial (x_i)_\alpha} \right) \quad , \tag{27}$$

and for the rotation rate tensor there is (almost identical to $\dot{\epsilon}_{\alpha\beta}$, except for the main minus sign inside the brackets)

$$(R_i)_{\alpha\beta} = \frac{1}{2} \sum_j \frac{m_j}{\rho_j} \left([(v_j)_\alpha - (v_i)_\alpha] \frac{\partial W_{ij}}{\partial (x_i)_\beta} - [(v_j)_\beta - (v_i)_\beta] \frac{\partial W_{ij}}{\partial (x_i)_\alpha} \right) \tag{28}$$

or

$$(R_i)_{\alpha\beta} = \frac{1}{2} \frac{1}{\rho_i} \sum_j m_j \left([(v_j)_\alpha - (v_i)_\alpha] \frac{\partial W_{ij}}{\partial (x_i)_\beta} - [(v_j)_\beta - (v_i)_\beta] \frac{\partial W_{ij}}{\partial (x_i)_\alpha} \right) \quad . \tag{29}$$

The final ingredient for completing the equation of motion is a convenient treatment of viscosity if desired or necessary. Generally speaking the forces acting on an element of the flow (which constitute the right-hand side of the equation of motion) are caused by internal stresses arising from deformation (in general described by the stress tensor), but also by the deformation's rate of change. The latter results in *viscous stress*, to be treated in principle alike stress described by the stress tensor $\sigma_{\alpha\beta}$. Several different ansatzes exist for implementing a so-called *artificial viscosity* in numerical schemes, Schäfer (2005) provides detailed information on this issue. A convenient treatment of viscosity has to be included in the energy-conservation equation (section 2.5) as well, in order to model the amount of dissipated energy in viscous flows.

2.5 Conservation of energy

The equation describing the conservation of energy, which is simply a representation of the first law of thermodynamics, can be stated for the mass-specific internal energy e as

$$\frac{de}{dt} = -\frac{p}{\rho} \frac{\partial v_\alpha}{\partial x_\alpha} + \frac{1}{\rho} S_{\alpha\beta} \dot{\epsilon}_{\alpha\beta} \quad , \tag{30}$$

where thermal dissipation due to viscosity is neglected. In the case of pure hydrodynamics the deviatoric stress tensor $S_{\alpha\beta}$ vanishes, and hence only the first term on the right-hand side remains.

Just as for the equation of motion various SPH representations exist for the energy-conservation equation as well. In practise it is important to use the same type of SPH-representation for both of them. Finally the transformation of (30) into the SPH scheme results in

$$\frac{de_i}{dt} = \frac{1}{2}\sum_j m_j \left(\frac{(\sigma_i)_{\alpha\beta}}{\rho_i^2} + \frac{(\sigma_j)_{\alpha\beta}}{\rho_j^2} \right) \left[(v_j)_\alpha - (v_i)_\alpha \right] \frac{\partial W_{ij}}{\partial (x_i)_\beta} \quad , \tag{31}$$

or alternatively

$$\frac{de_i}{dt} = \frac{1}{2}\sum_j m_j \frac{(\sigma_i)_{\alpha\beta} + (\sigma_j)_{\alpha\beta}}{\rho_i \rho_j} \left[(v_j)_\alpha - (v_i)_\alpha \right] \frac{\partial W_{ij}}{\partial (x_i)_\beta} \quad , \tag{32}$$

as analogues of (24) and (25) respectively. The definition and computation of the stress tensor $\sigma_{\alpha\beta}$ has already been described in section 2.4. For involving a convenient treatment of viscosity the reader is also referred to section 2.4 and again to Schäfer (2005), respectively.

2.6 Equation of state

In order to close the system of equations for either the hydrodynamic or the full solid-body treatment, an equation of state (eos) provides information on a material's behavior and connects the thermodynamic quantities pressure p, density ρ, and internal energy e (or temperature, respectively). A simple example would be the ideal gas law. An overview of eos used for impact and collision simulations is provided for example by Melosh (1989).

A widely used, non-linear eos was introduced by Tillotson (1962), originally for high-velocity impacts. It utilizes 10 different parameters and distinguishes three different domains, (1) compressed regions and cold expanded states, with internal energies less than the energy of incipient vaporization e_{iv}, (2) expanded regions with internal energies above the energy of complete vaporization e_{cv}, and (3) intermediate states where the pressure is interpolated linearly. Summarized the Tillotson eos can be stated as

$$p(\rho, e) = \begin{cases} \left[a + \frac{b}{\frac{e}{e_0 \eta^2} + 1} \right] \rho\, e + A\, \mu + B\, \mu^2 & e < e_{iv} \\ a\, \rho\, e + \left[\frac{b\, \rho\, e}{\frac{e}{e_0 \eta^2} + 1} + A\, \mu\, \mathrm{e}^{-\beta \left(\frac{\rho_0}{\rho} - 1 \right)} \right] \mathrm{e}^{-\alpha \left(\frac{\rho_0}{\rho} - 1 \right)^2} & e > e_{cv} \end{cases} \quad , \tag{33}$$

with $\eta = \rho / \rho_0$ and $\mu = \eta - 1$, where ρ_0 is the density at zero pressure. It can be applied in a relatively wide range of physical conditions, while being computationally simple. All computations presented throughout this thesis were performed with the Tillotson eos as given in (33), using parameters for basalt and ice presented in Benz and Asphaug (1999).

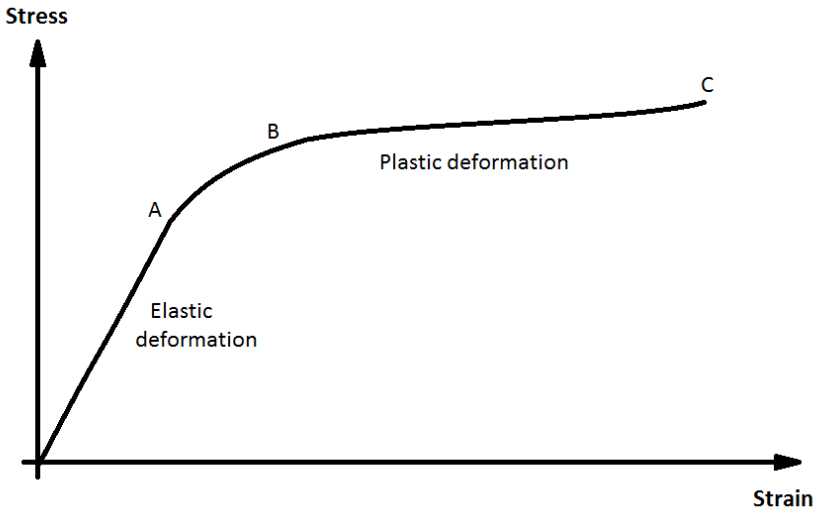

Figure 2 Schematic illustration of a typical stress-strain curve. For sufficiently small applied stresses the relation is close to linear (Hooke's law). Beyond point A the linearity breaks down but the deformation is still elastic up to point B. For applied stresses larger than at B the deformation becomes plastic, molecular bonds break and rearrange, thus changing the body's shape permanently, even if all applied stresses vanished again. For even higher stresses the material eventually experiences brittle failure and breaks at point C. Considering this behavior allows to distinguish between ductile and brittle materials, where brittle material exhibits much less (or none at all) plasticity.

2.7 Plasticity and brittle failure of solid bodies

In addition to the elastic regime, where Hooke's law applies as already described in section 2.4, the behavior of solid bodies in general doesn't fit this simple linear description anymore once sufficiently large stresses occur. *Figure 2* schematically depicts this behavior, where – with increasing strain – the elastic region is followed by plastic behavior before brittle failure sets in eventually.

In order to model plastic behavior (of isotropic material) the *von Mises yielding criterion* is used for all simulations presented here (see Benz and Asphaug, 1994). It is based on reducing the deviatoric stress tensor by

$$S_{\alpha\beta} = f S_{\alpha\beta} \tag{34}$$

once a certain yield stress (yield limit) is applied. This marks the onset of plastic behavior. The reducing factor f is given by

$$f = \min\left(\frac{Y_0^2}{3\,J_2}, 1\right) \quad , \tag{35}$$

where Y_0 denotes the yield stress, which depends – besides the material – also on other quantities like temperature. Finally J_2 is the second invariant of $S_{\alpha\beta}$, given via

$$J_2 = \frac{1}{2} S_{\alpha\beta} S_{\alpha\beta} \quad . \tag{36}$$

The final step in modeling solid-body behavior is to account for material fracture once a certain level of stress occurs (point C in *Fig. 2*). Looking at the underlying physics it becomes evident that fracture is related to failure of molecular bonds, or – more precisely – to flaws in the atomic lattice. Indeed, experiments show that the actual material strength is significantly lower than the theoretically derived one (assuming a perfect lattice), indicating that cracks in the material start to grow just at these flaws – once tensile forces become sufficiently high to *activate* them. The Lagrangian nature of SPH makes it relatively easy to follow the crack development, in particular compared to Eulerian approaches. Benz and Asphaug (1995) introduced a model for brittle failure to SPH, which is based on a continuum model of fracture by Grady and Kipp (1980). This model in turn is based on a flaw (probability-) distribution derived by Weibull (1939), giving the number of flaws per volume n with activation thresholds (strains) lower than ϵ via a simple power law

$$n(\epsilon) = k\,\epsilon^m \quad , \tag{37}$$

where k and m are material-dependent parameters. More precisely (37) specifies the cumulative number of flaws (per unit volume) up to a certain threshold strain ϵ. In practice the flaws (i.e. their activation thresholds) have to be assigned to the SPH particles prior to the simulation run. This can easily be done by processing the cumulative distribution (37) *from the left*, i.e. from low towards high threshold strains. This can be achieved by demanding

$$k\,\epsilon_i^m\,V = i \tag{38}$$

with $i = 1, 2, 3, \ldots$, where the left-hand side gives the number of flaws with thresholds lower than ϵ in the overall considered volume V. Successively inserting increasing i-values here means to demand the number of flaws below ϵ_i to be exactly 1, then 2, and so forth. Rearranging equation (38) to

$$\epsilon_i = \left(\frac{i}{k\,V}\right)^{1/m} \tag{39}$$

eventually allows for calculating a large number of (increasing) threshold strains ϵ_i by successively inserting $i = 1, 2, 3, \ldots$, which can then be each assigned to a randomly picked SPH particle. E.g. $i = 42$ gives the ϵ where exactly 42 flaws are supposed to have lower ϵ-values. Since $\epsilon_1, \epsilon_2, \ldots, \epsilon_{41}$ have already been assigned to particles while processing $i = 1, 2, \ldots, 41$, ϵ_{42} gives just *one* further threshold strain to be assigned to another randomly picked particle. This procedure has to be repeated until each particle has been assigned at least one threshold strain, to avoid indestructible regions. An interesting consequence of this procedure is the possibility to straight-forwardly introduce (pseudo-) random elements into a simulation run's initial conditions, by simply using different seeds in otherwise identical setups, or on the other hand to entirely avoid this by not adjusting the seed in successive computations.

The next step in the damage model is to relate these scalar threshold strains to the – in general rather complicated – local stress state of the material. One possible ansatz by Melosh et al. (1992) is to obtain the maximum tensile stress from the principal stresses $\sigma_1, \ldots, \sigma_3$ (computed by a principal axis transformation) via $\sigma_{max} = \max(\sigma_1, \sigma_2, \sigma_3)$, where the stress tensor might be already reduced by damage and yielding. This result

is then used to calculate the local scalar strain following

$$\epsilon = \frac{\sigma_{max}}{(1-D)\,E} \quad , \tag{40}$$

with Young's modulus E calculated from the bulk and shear moduli K and μ via

$$E = \frac{9\,K\,\mu}{3\,K+\mu} \quad . \tag{41}$$

The so-called *damage* D is a scalar parameter $\in [0,1]$, where $D=0$ corresponds to an undamaged region, where the local scalar strain (40) has never increased to even the lowest activation threshold associated with that SPH particle, and $D=1$ represents a region where the material can be considered entirely ripped apart and hence feels no tensile and shear stresses anymore at all. An entirely damaged material therefore behaves in many ways like a fluid. The influence of the damage on the stress tensor $\sigma_{\alpha\beta}$ can in general be expressed as

$$\begin{aligned} (\sigma_d)_{\alpha\beta} &= -p_d\,\delta_{\alpha\beta} + (1-D) S_{\alpha\beta} \\ p_d &= \begin{cases} p & p \geq 0 \\ (1-D)\,p & p < 0 \end{cases} \quad , \end{aligned} \tag{42}$$

i.e. all components except for (positive) pressure are reduced by a factor $(1-D)$.

As soon as the local strain reaches a flaw's activation threshold strain, a crack emerges and is assumed to grow with a constant velocity c_g. The volume where stress is released due to a growing crack is well approximated by its circumscribing sphere (Walsh, 1965) as $V_r = 4/3\,\pi a^3$, with the crack's half length a. The local damage is then defined as the ratio of the released volume to the total (sub-)volume considered for growth of the individual crack $V_s = 4/3\,\pi R_s^3$, thus

$$D = \frac{V_r}{V_s} = \frac{a^3}{R_s^3} \quad . \tag{43}$$

Taking the derivative w.r.t. time and considering $c_g = da/dt$, this leads to a simple differential equation for the development of the local damage $d(D^{1/3})/dt = c_g/R_s$. However, to also take the accumulation of cracks into account, a modified version thereof is used, namely

$$\frac{d(D^{1/3})}{dt} = n_{act}\frac{c_g}{R_s} \quad , \tag{44}$$

where the number of already activated flaws n_{act} contributes to the amount of damage growth. Since a certain sub-volume (SPH particle) contains in general more than one flaw it has to be ensured that the damage does not grow beyond an amount supported by the currently activated number of flaws and specifically that $D<1$ unless *all* flaws are activated. In order to achieve this, the maximum attainable damage via (44) is limited by the ratio of activated to total flaws following

$$D_{max}^{1/3} = \frac{n_{act}}{n_{tot}} \quad . \tag{45}$$

3 Initial conditions and relaxation method

In order to be able to apply the SPH formalism and to advance a collection of SPH particles from each timestep to the next one, an appropriate initial state of the system of particles has to be specified and generated in the first place. These start values – positions, velocities and all other relevant characteristics of each particle – are then fed to the SPH simulation program as initial conditions. Since the final outcome of a simulation run depends, of course, directly on them, it is important to pay enough attention to this issue in order to produce meaningful results. An ideal initial configuration of SPH particles has to fulfill (at least) the following conditions:

- Isotropy
- Low particle noise
- Equilibrium state
- Resemble reality
- Easy to implement and fast to generate

The first requirement, *isotropy*, is mainly a geometrical issue. The spatial arrangement of SPH particles itself should not have any preferred directions. A good counterexample is the probably most simple particle configuration one can come up with, the simple cubic lattice, where particles are strongly aligned especially along three major axes. This strong anisotropy can give rise to unphysical behavior, for example when it comes to differences in the propagation of sound waves and shocks along these directions compared to others. This geometrical requirement, along with the next point – the problem of particle noise – are described and summarized comprehensively by Diehl et al. (2012). In general all regular lattice configurations can cause numerical artifacts, like the mentioned effects caused by unphysical symmetry.

The term *particle noise* refers – in the context of SPH – to local inhomogeneities in the particle distribution. The concept becomes immediately clear when considering a particle arrangement produced with random particle positions (see the central panel in *Fig. 3*) for modeling a constant-density material. The local deviations from homogeneity in such a randomly-chosen configuration then in turn introduce numerical fluctuations in physical quantities. The SPH method, as described in section 2, of course requires low noise because of its very nature, i.e. due to the principle of replacing quantities by weighted averages of their neighboring particles. Regular lattice configurations naturally exhibit very good characteristics in this respect, while for other particle arrangements more care has to be taken to ensure low noise levels. Topics related to the geometrical arrangement of SPH particles are covered in detail in section 3.1.

Demanding the initial configuration to be in an *equilibrium state* does of course *not* refer to the simulation domain as a whole, but rather to certain subcomponents, otherwise there would be no time evolution at all. Depending on the individual problem, often at least some individual parts of the overall domain should initially be in equilibrium. A good example to illustrate this are simulations of giant collision outcomes, where each one of the colliding protoplanets should initially be in (mechanical) equilibrium, while the whole system (consisting of the 2 bodies) is typically not.

Resemblance of reality could be considered as *the* requirement for good initial conditions, i.e. being understood as already including all the other of the above points (except for the last one). However, here it shall *not* be considered this broad umbrella term, but rather in a more physical way, meaning a proper allocation of physical quantities to the SPH particles. Thinking again of planetary-sized bodies, this would mean to accurately model their internal structure (e.g. density, pressure and internal energy) prior to the start of the actual simulation run. Since it is usually the aim of numerical simulations to model objects as close to reality as possible this point is of crucial importance. Possible methods of producing equilibrium initial conditions that resemble reality are discussed in section 3.2 with a focus on giant collision simulations.

Finally the algorithm for producing the initial particle configuration should be *easy to implement* and it should be able to *generate it fast*, i.e. in little computing time. Even though these criteria can be considered favorable in general, the requirements might be put into perspective in certain situations. The still acceptable efforts for implementation may strongly depend on the volume of the underlying scientific endeavor, and the required computing time to generate them will be assessed relative to the machine time of the SPH simulation program itself.

Even though these 5 points are in principle necessary conditions for every given SPH simulation's initial state, it is usually neither possible to perfectly match them all, nor is it convenient to bullheadedly follow each point strictly, at least not for all problems.

3.1 Initial particle arrangement

Choosing a proper spatial initial distribution of SPH particles is an important point for various aspects, like minimizing symmetry effects and particle noise, as mentioned in the previous section. Various possibilities have been proposed and are in use, each one with its own advantages and drawbacks. This section presents an overview along with some illustrating examples, before focusing particularly on giant collision scenarios, and thus on spherical particle distributions.

3.1.1 Geometrical structure

The initial geometrical arrangement of SPH particles can potentially have a crucial impact on the overall simulation outcome. Probably the first thing that comes to mind when attempting to fill a given volume with SPH particles are regular lattice configurations. Especially two distinct possibilities are important in this context, namely the simple cubic (SC) and either one of the two optimal packing schemes for equal spheres[7], which are the cubic close-packed (CCP) and hexagonal close-packed (HCP) lattice. The latter two are obtained by starting with one layer (A) of close-packed spheres (in a hexagonal manner) followed by stacking a similar layer (B) at one of the two possible positions, while the next (third) layer is placed directly above A *or* at the third possible relative position (C). The stacking sequence ABAB... results in a HCP lattice, while ABCABC... leads to a CCP configuration. While setting up a SC lattice is trivial, these two can be viewed as consisting of regular tetrahedrons (with vertices at the sphere's centers), strung together until the desired volume of space is filled. Another possibility

[7] In three-dimensional space the densest possible packing of equal spheres results in a packing fraction of approximately 0.74, with 12 direct neighbors for every sphere.

is to start with a row of spheres, successively add additional rows (densely packed) until the desired two-dimensional extent is covered, and finally copy and move these layers according to the above described patterns for HCP or CCP. *Figure 3* shows these three configurations in the first row, along with various different possibilities of arranging particles to end up with a sphere.

While the SC lattice is very simple to set up, it suffers some severe drawbacks. An important thing to note is that it does not represent a stable equilibrium distribution of particles. It exhibits very strong anisotropy, and therefore preferred directions (locally and globally), especially along the three major axes. As a consequence strong symmetry effects can be expected (Diehl et al., 2012).

Unlike in the SC case, HCP and CCP lattices represent stable equilibrium configurations. In principle they suffer from regularity in their arrangement as well, but the preferred directions are much less pronounced. The HCP and CCP configurations behave very similar in general (Diehl et al., 2012). When it comes to particle noise all these lattice configurations are very advantageous, due to their regular structures, compared to non-regular choices.

Besides these relatively simple regular lattice configurations there are also various other possibilities – *Fig. 3* illustrates a selection of these for comparison. So far all the arrangements described were spatially uniform. Beyond that a configuration can also be set up to be spatially adaptive, e.g. particle distances increasing with the radial coordinate in a sphere, which will not be discussed further here.

3.1.2 Rotation into arbitrary position

If one chooses a regular lattice structure to set up a SPH simulation's initial configuration, symmetry effects due to anisotropy can become a significant drawback. Besides the right choice of the lattice structure, like using HCP or CCP instead of SC, a slight relative rotation of parts of the simulation domain can help to further reduce symmetries in some cases. For the special case of a collision simulation of two spheres (e.g. protoplanets) this can be realized by rotating the spherical initial configurations relatively to each other, by angles not directly present in the lattice itself, to avoid replacing one symmetry by another. This can be considered a measure of reducing global anisotropy. In practice this can be achieved by applying suitable rotation matrices. For the respective rotations about the z-, y- and x-axis and in three dimensions they are given by:

$$
\begin{aligned}
R_z(\theta) &= \begin{pmatrix} \cos\theta & -\sin\theta & 0 \\ \sin\theta & \cos\theta & 0 \\ 0 & 0 & 1 \end{pmatrix} \\
R_y(\theta) &= \begin{pmatrix} \cos\theta & 0 & \sin\theta \\ 0 & 1 & 0 \\ -\sin\theta & 0 & \cos\theta \end{pmatrix} \quad . \\
R_x(\theta) &= \begin{pmatrix} 1 & 0 & 0 \\ 0 & \cos\theta & -\sin\theta \\ 0 & \sin\theta & \cos\theta \end{pmatrix}
\end{aligned} \tag{46}
$$

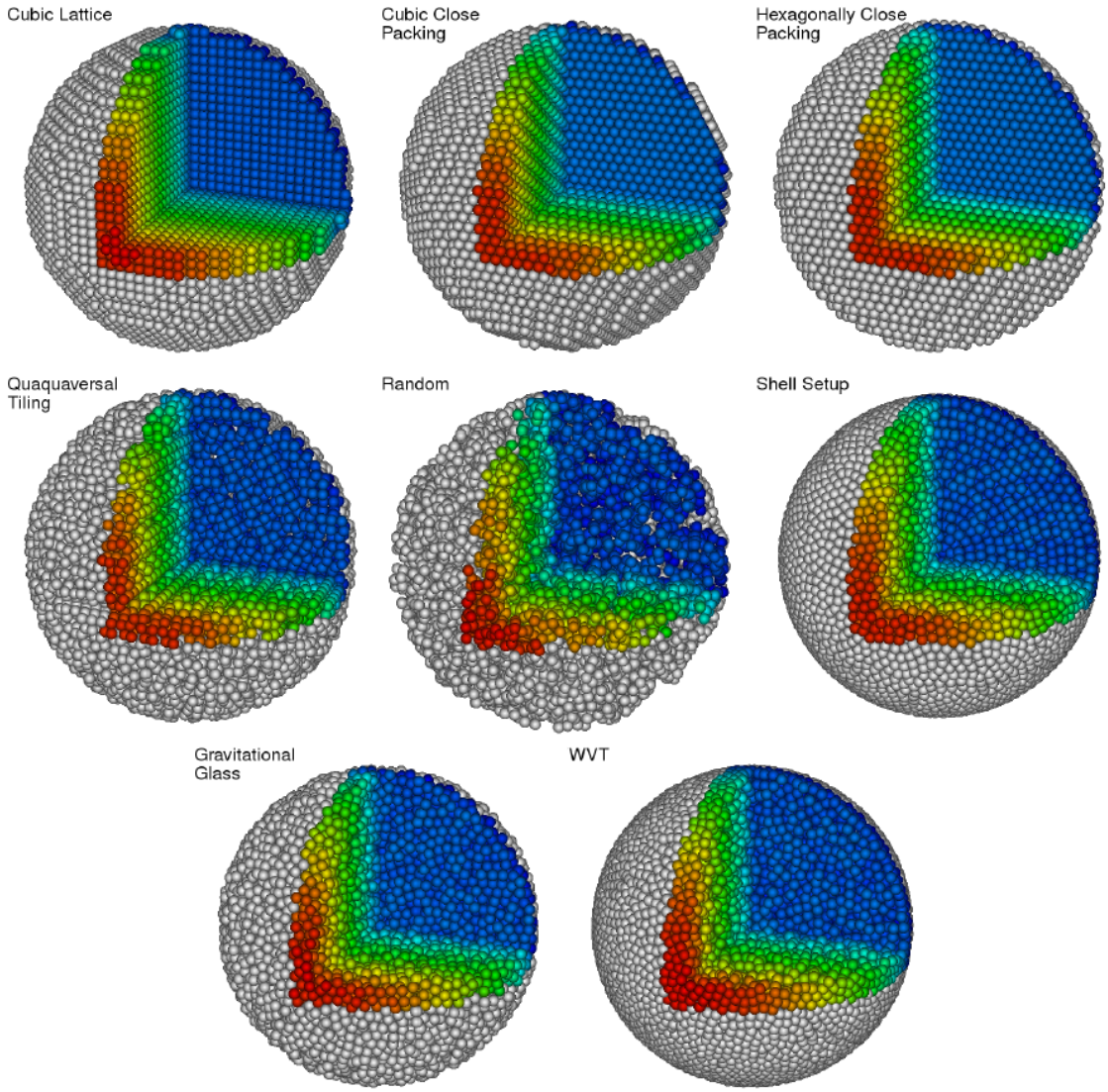

Figure 3 Illustration of different possibilities for setting up (equal) particles in a sphere. The three configurations in the first row are those discussed in the text, where the close resemblance of the CCP and the HCP lattice are clearly visible. The other arrangements represent different possibilities, partly with significantly differing properties. Quaquaversal Tiling is another lattice-like configuration, the shell setup arranges particles in concentric shells, gravitational glass results from damped particle motion with inverted gravity, and WVT utilizes weighted Voronoi tesselations. Approximately 22000 particles constitute each sphere. One quadrant is cut out in each case to give a better impression of the internal particle arrangement, and the colors should provide a better 3-d depth. Refer to the original paper for a detailed explanation of the configurations not discussed here. Courtesy of Diehl et al. (2012).

These representations define *extrinsic rotations* with θ being the respective angle of rotation. This means that the rotations are carried out about the always fixed (initial) coordinate axes, where – assuming a right-handed coordinate system and θ positive – the direction of rotation follows the right-hand rule with the thumb pointing towards the considered coordinate axis.

Since one component remains unchanged in each case (z-component for rotation about z-axis, etc.), it is in practice entirely sufficient to apply only the respective 2x2 versions in order to save computing time.

3.1.3 Testing symmetry effects in (simulated) reality

In order to demonstrate the impact of the initial geometrical arrangement of SPH particles, a specific collision scenario was chosen and investigated using various different such initial configurations. The two colliding bodies in this scenario have equal masses of 10^{20} kg each[8], where one consists of pure basalt, while the other comprises a basalt core and an ice shell with a mass fraction of 0.3. They are performing a perfect head-on collision with a velocity of 0.75 km/s, hence a radially symmetric disk-like distribution of material would be expected when looking directly into the direction of collision, at least in the (homogeneous) continuum limit.

Based on this scenario, *Fig. 4* shows a comparison between an implementation using a SC lattice without any initial rotation (left panels) and on the other hand a more sophisticated, initially rotated HCP configuration (right panels, see the caption for more details). The figure shows the collision from the point of view of an observer directly behind the basalt-water body, looking straight into the direction of relative motion. This is the reason why in the two upper pictures almost only ice particles (white) are visible, where the SC structure as well as the rotated HCP configuration can be clearly distinguished. Proceeding to an advanced time in the simulation run (middle panels) already shows some symmetry effects. The SC initial condition tends to produce global structures that reflect the symmetries of this lattice configuration, while the rotated HCP structure is significantly closer to being isotropic. In addition the SC run produces a clearly diamond-shaped particle distribution at this stage, in contrast to the close to circular appearance for the HCP lattice. The two bottom panels in *Fig. 4* finally show a later stage of the simulation, when most of the material disk has settled into a roughly spherical configuration again, due to gravity. Immediately apparent differences can be found in the remaining debris disk around the central bodies where the strong preferred directions of the SC lattice result in lines of dense material along the main symmetry axes, while other directions are much less populated (lower left panel). Since the rotated HCP initial configuration also constitutes a regular lattice, numerical artifacts of that kind are present in its outcome as well, but they are weaker and their directions – if discernible – seem more random (lower right panel). These pictures are, however, not only the result of direct initial asymmetries but, to some extent, also of subsequent gravitational clumping along these asymmetries. Another important difference in this third examined timestep are the central bodies' properties. The mass that went into the merged body compared to the mass of ejected material is often of particular interest when running such a collision simulation. While for the SC case a mass of about 1.28×10^{20} kg can be

[8] This is about one-tenth of the mass of *Ceres*, the largest object in the main asteroid belt.

found in the central body, it is 1.56×10^{20} kg for the rotated HCP initial configuration. Considering the overall simulated mass of 2×10^{20} kg this translates to considerably different mass fractions of 0.64 and 0.78 respectively. A notable difference can also be found in the distribution of the materials (ice/basalt), where the mass fractions of ice in the central body and the debris disk differ significantly from the SC to the HCP case. This could be particularly interesting for investigations concerning water transport and the amount of water that is lost to space during a collision. In this specific example the central body at this stage is not only more massive when the simulation was started with the rotated HCP lattice, but its ice mass fraction is also higher, summing up to the cumulative result of considerably lower amounts of water/ice lost to the surrounding material. Additionally there are also notable differences in other global quantities, like overall kinetic energy, indicating possible differences in the (further) kinematic evolution of the scenario.

To elaborate on this and to gain more insights into the impact of the initial particle arrangement, *Fig. 5* illustrates the outcome of two simulation runs, where now both start with a HCP lattice, but one without (left panels) and the other one with an initially rotated configuration (right panels, see the caption for more details), allowing to investigate the effects of an initial rotation on reducing symmetry effects. The underlying scenario is identical to the above one, which means that the rotated HCP simulation run is in fact exactly the same one as before. The point of view and the output times represented by the snapshots are also identical to *Fig. 4*. The two upper panels again show the simulations' initial states, making the different orientation in space clearly visible. The differences in the middle panels are weaker than in the corresponding panels in *Fig. 4*, but nevertheless some symmetry effects in the particle alignment as well as a global diamond-shape can again be observed in the not rotated configuration, while these effects seem smaller or even non-existent when including initial rotation. The bottom panels finally indicate that the lines of denser material in the remaining debris disk are slightly more pronounced and rather aligned with the symmetry axes in the left picture, compared to more random orientations in the right snapshot. Concerning the central bodies' masses and the ice mass fractions no significant difference was found in this case. This particular example indicates that symmetry effects can indeed be further reduced by applying an initial relative rotation to the colliding bodies, even though the effects are more subtle compared to the great improvement introduced by the step from a SC to a HCP lattice. Finally, a direct comparison of the respective bottom left panels in *Fig. 4* and *Fig. 5* illustrates the improvement by simply using a HCP lattice instead of a SC one (and not applying an initial rotation for further enhancement). The weaker preferred directions of the HCP configuration basically result in much weaker symmetry effects.

Besides the specific scenario presented and discussed in this section the impact of varying its major parameters has been considered as well. The main parameters constituting the scenario are the masses of the colliding bodies, their (material) composition, the impact geometry and the impact velocity. The value of the velocity was chosen basically in a way that the colliding bodies get entirely disrupted with considerable amounts of dispersed material, while for too low choices it would be more difficult to directly observe most of the above found symmetry effects. The geometry of the impact was chosen to be head-on based on very similar reasoning, namely that observing and characterizing

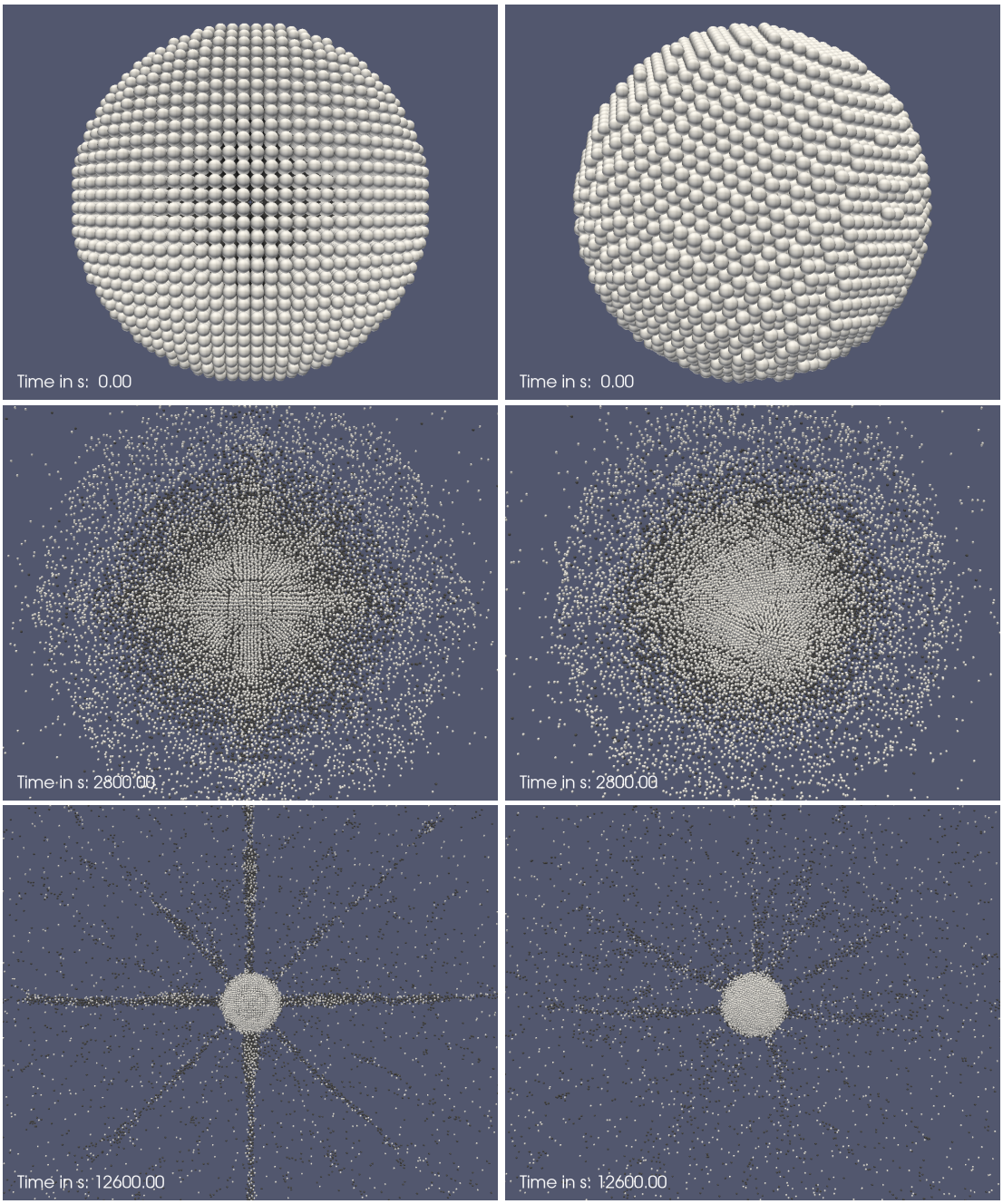

Figure 4 Identical collision scenarios implemented with a SC lattice without rotated initial configuration (left panels) and a HCP lattice with rotated initial configuration (right panels). Each of the two colliding bodies has 10^{20} kg, one consisting of pure basalt (black particles) and the other one having an ice shell (white particles) with 30% its mass. Approximately 25000 SPH particles were used per scenario. The head-on collision with 0.75 km/s is seen from directly behind the water-rich body. The two bodies of the HCP lattice configuration are initially rotated by angles of $20°/20°/20°$ and $-20°/-20°/-20°$, respectively (while the SC bodies are not rotated; cf. section 3.1.2 for details on the initial rotation). Refer to the text for a detailed discussion.

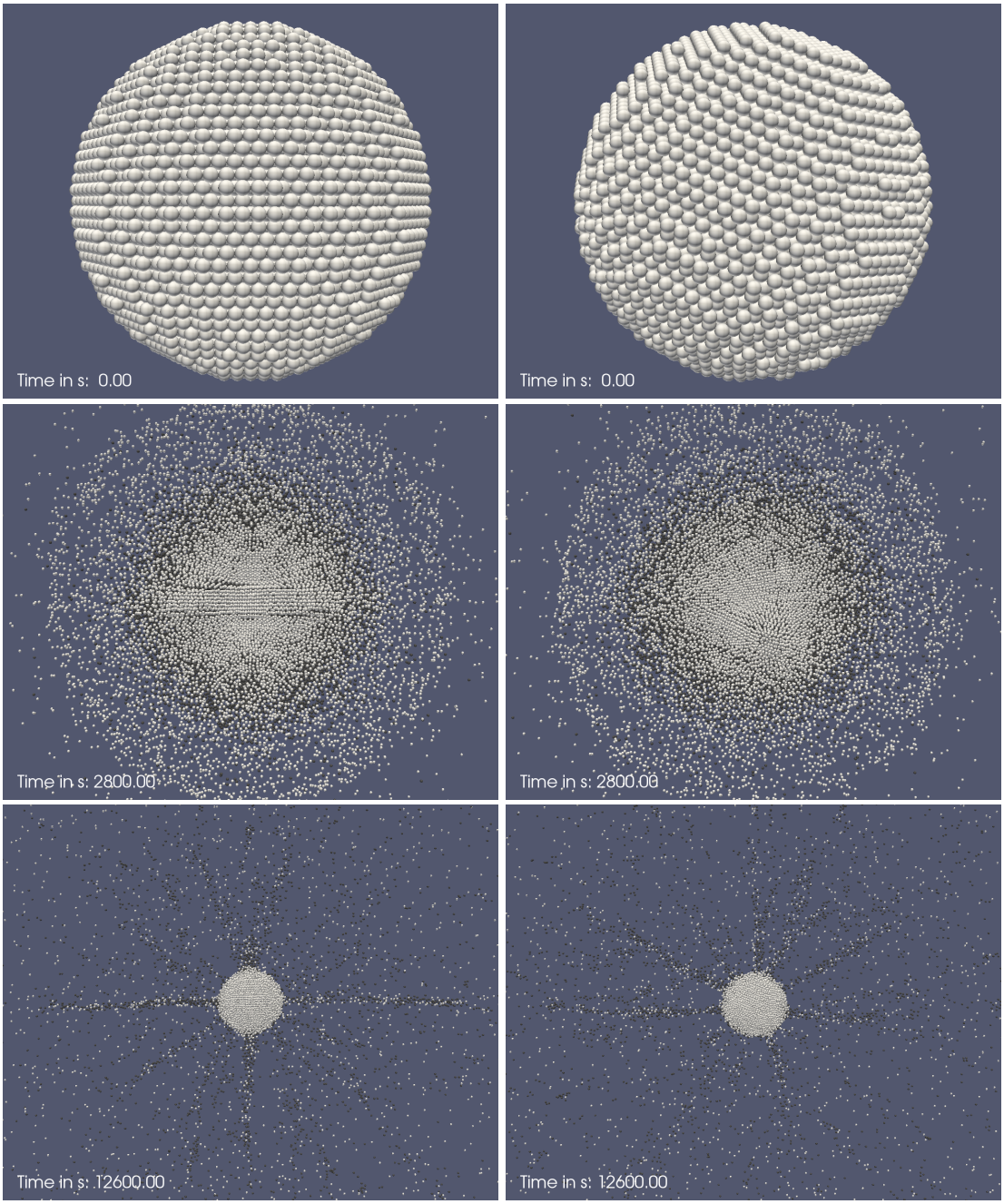

Figure 5 Identical collision scenarios implemented with a HCP lattice without rotated initial configuration (left panels) and a HCP lattice with rotated initial configuration (right panels). The basic setup is essentially the same as in *Fig. 4*: Each of the two colliding bodies has 10^{20} kg, one consisting of pure basalt (black particles) and the other one having an ice shell (white particles) with 30% its mass. Approximately 25000 SPH particles were used per scenario. The head-on collision with 0.75 km/s is seen from directly behind the water-rich body. The two bodies in the right simulation run are initially rotated by angles of $20°/20°/20°$ and $-20°/-20°/-20°$, respectively (while the bodies in the left run are not rotated; cf. section 3.1.2 for details on the initial rotation). See the text for a discussion.

the expected effects is easiest with a priori knowledge of the ideal (theoretical) shape of the simulation outcome. For the implemented head-on collision, and assuming homogeneous material, this would be a simple radially symmetric disk-like structure, while different impact geometries would result in more complicated shapes, with nevertheless comparable symmetry effects expected, even though harder to observe. The bodies' composition was chosen to represent a typical configuration with one being purely rocky, made of 100% basalt, while the other one, possessing a basalt core and a 30% ice shell, is similar in composition and structure to well-known solar system objects with large ice mass fractions. Besides being a rather typical scenario in terms of composition, using two different materials particularly provides the possibility to track each one of them individually. The case of water as the minor constituent (with an overall mass fraction of only 0.15) is in addition of particular interest for addressing questions concerning water transport during collisions. The above considerations of water mass fractions when starting with a SC compared to a HCP lattice (cf. *Fig. 4* and the text) give an impression of that. The bottom line is that no big change in the observed symmetry effects can be expected when using different compositions, albeit they might be harder to track.

The last important parameter in this context is mass. When performing similar investigations on significantly larger (more massive) colliding bodies the differences between the initial configurations is much less discernible, probably because self-gravity is too strong then. The strong symmetry effects in a SC arrangement lead to visible effects similar in strength as those caused by more arbitrary density fluctuations when starting with an (initially rotated) HCP lattice. This means that there is still expected to be a considerable difference in terms of symmetry effects but it is not as easily visible anymore when going for more massive bodies. A quite similar effect comes into play when using significantly smaller bodies, where self-gravity is probably just too weak to sufficiently enhance appearing symmetry effects to make them as clearly visible as it is the case for the scenario above, with body masses of 10^{20} kg each. The conclusion is that self-gravity in a scenario with approximately the above masses has the right magnitude to enhance the strong symmetry effects of the SC lattice sufficiently, but not too much the (more) arbitrary effects in the (initially rotated) HCP configuration.

Finally one can say that the investigated scenario does not just represent some pathological set of parameters leading to these clear symmetry effects, but rather that this choice of parameters makes them clearly visible and easy to investigate, while they are, to some extent, present in most other scenarios, including non-spherical particle distributions, as well.

3.2 Relaxation

The last section gave an overview of how the initial geometrical arrangement of SPH particles (i.e. their positions) affects the quality of an initial configuration and thus the validity of the simulation outcome. The goal was to minimize symmetry effects that emerge from weaknesses in this initial configuration. In order to produce meaningful simulation results another major point is typically to ensure that the initial state is *relaxed*. This means that to end up with a good initial configuration it is important to set up a system of particles with individual properties in a way that this system is in a *self-consistent equilibrium state that resembles reality*. In this context *self-consistent* basically refers to the initial condition being set up as close as possible to a configura-

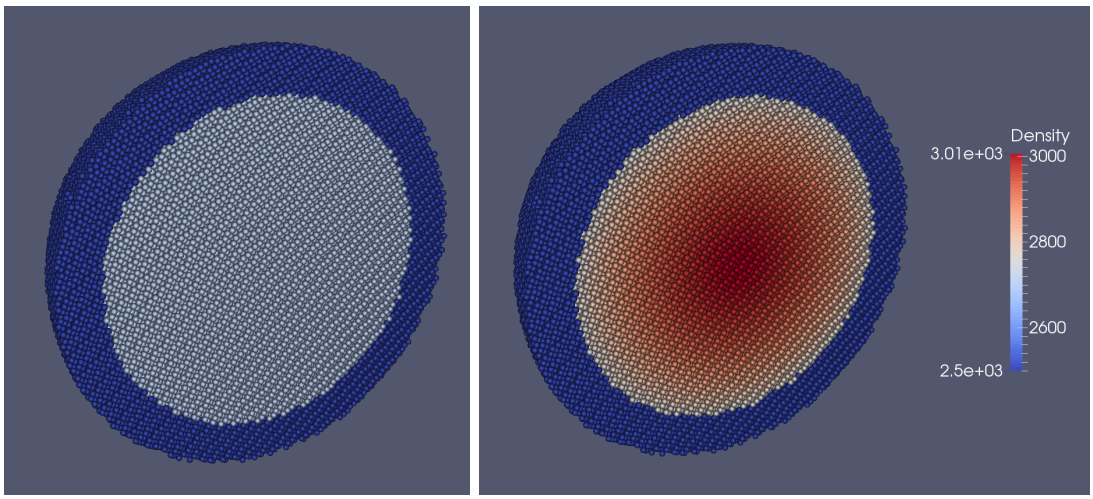

Figure 6 Interior density structure of a 1 Moon-mass (7.35×10^{22} kg) body with homogeneous density throughout the core and shell (left panel) versus its relaxed counterpart (right panel). Both bodies consist of a basalt core and an ice shell (with a mass fraction of 0.25) with uncompressed densities of 2700 kg/m^3 and 917 kg/m^3, respectively. The color coding, valid for both bodies, was chosen to emphasize the density structure in the relaxed body's core, while the variations in its shell are not visible. Among the significantly varying parameters is the overall radius with values of 2130 km (left) and 2100 km (right), respectively.

tion that would emerge from the underlying SPH algorithm itself. Since it is a basic requirement to the applied SPH scheme to reproduce the laws of physics accurately, this translates directly to the demand for resemblance of reality. Just a different aspect of this is that usually at least some parts of the overall simulation domain should initially be in (mechanical) equilibrium. With the focus on giant collisions – and thus on planetary-sized bodies – this means in particular each of the colliding bodies, while the whole system (of the two bodies) is typically not. In this respect equilibrium can be understood as each individual body having settled into a (spherically-shaped) state of rest, exhibiting a certain internal structure of density, pressure and internal energy, where no unphysical oscillations appear anymore. An illustrative example of this can be seen in *Fig. 6*, showing a body of 1 Moon-mass with a homogeneous-density core and shell versus its fully relaxed counterpart. Besides the obvious differences in the internal structure (see *Fig. 10* for the relaxed body's internal structure) and the fact that the unrelaxed version would start to contract and oscillate once the simulation program is started (cf. section 3.2.1, and particularly *Fig. 7*), there are also considerable differences in parameters like the core and shell dimensions. It is obvious that these two representations could potentially lead to significant deviations in the outcome of a simulation run when used as initial conditions. In the following the common numerical approach for relaxation is presented first (section 3.2.1), before a *semi-analytical* approach is introduced and discussed as an alternative to that in section 3.2.2. In the final part (section 3.2.3) the semi-analytical approach is validated, and the importance of relaxation itself is studied for a broad range of masses, which are of particular importance in the context of planet formation.

3.2.1 Numerical approach

One popular possibility for producing relaxed initial configurations is by numerical means. The idea behind this is rather simple, particularly when setting up initial conditions for giant collision simulations. Basically it means to construct a body of homogeneous (i.e. w.r.t. density, etc.) regions, typically a shell structure made up of different materials, and put it (alone) in the SPH simulation program. Gravity starts acting on it, tending to compress initially uncompressed regions, forcing the whole body to collapse. Due to inertia, this inwards movement of material continues even beyond the point of hydrostatic equilibrium, i.e. where gravity were balanced by a pressure gradient, resulting finally in a damped (radial) oscillation of the whole body. This process leads to a transformation of the gravitational energy stored in the initial, homogeneous-density body, into thermal energy and mechanical (compression) energy, usually summarized as internal energy. Once the oscillation ends (and a final equilibrium state is reached), a certain internal structure will have emerged, representing hydrostatic equilibrium. In addition the procedure automatically results in a self-consistent state, since it is the result of the very same SPH algorithm it will be fed to again, together with the (also relaxed) rest of the simulation domain (usually the second body) when starting the actual simulation run. *Fig. 6* provides a visualization of the starting and the end point of this procedure by showing the general appearance (in terms of density) of the homogeneous initial state compared to its relaxed counterpart (corresponding to internal structures similar to *Fig. 8*). An illustration of the process itself is provided in *Fig. 7*, where the radial oscillations of 3 different bodies – with the same bulk composition but distinct masses – are depicted. Each of the bodies consists of a basalt core and a shell made up of ice, with a mass fraction of 0.25. Their overall masses where chosen to represent typical values for planetary embryos and protoplanets[9], being those of Ceres, the Moon, and the (geometric) mean of the two (cf. *Tab. 1*). Since the plots in the figure are all normalized to the same (arbitrary) computing time unit, a direct comparison is possible. The naked eye impression that the required computing time increases significantly with increasing mass is proven by a more detailed analysis. In order to further extend the data set and to cover a wider mass range two additional scenarios have been invoked, comprising masses of a tenth of Ceres' and ten times the Moon's respectively, with the bulk composition remaining unchanged. A summary of the considered scenarios is provided in *Tab. 1*, along with the initial oscillation amplitude, the final (relaxed) radius and two evaluated time scales for a quantitative assessment of the required computational resources. The obvious similarity to damped oscillations gives rise to the first time scale, denoted *exponential decay time* (τ_d), being the time required for the oscillation amplitude to decrease by a factor $1/e$ (determined starting at $t = 0$), thus measuring the oscillation's rate of decay. Even though no continuous trend can be observed for the considered mass range, there is a considerable difference between the lower- and the higher-mass scenarios. A closer examination shows that this rather non-continuous behavior can be at least partly attributed to the underlying numerics, in particular to the adaptive time integration used for the simulations presented here, with the computing time being approximately proportional to the number of integrator steps performed per

[9] Since there is no clear, widely accepted definition of these terms they are used when referring to bodies with masses roughly ranging from Ceres up to the Moon here, and – for the sake of simplicity – interchangeably.

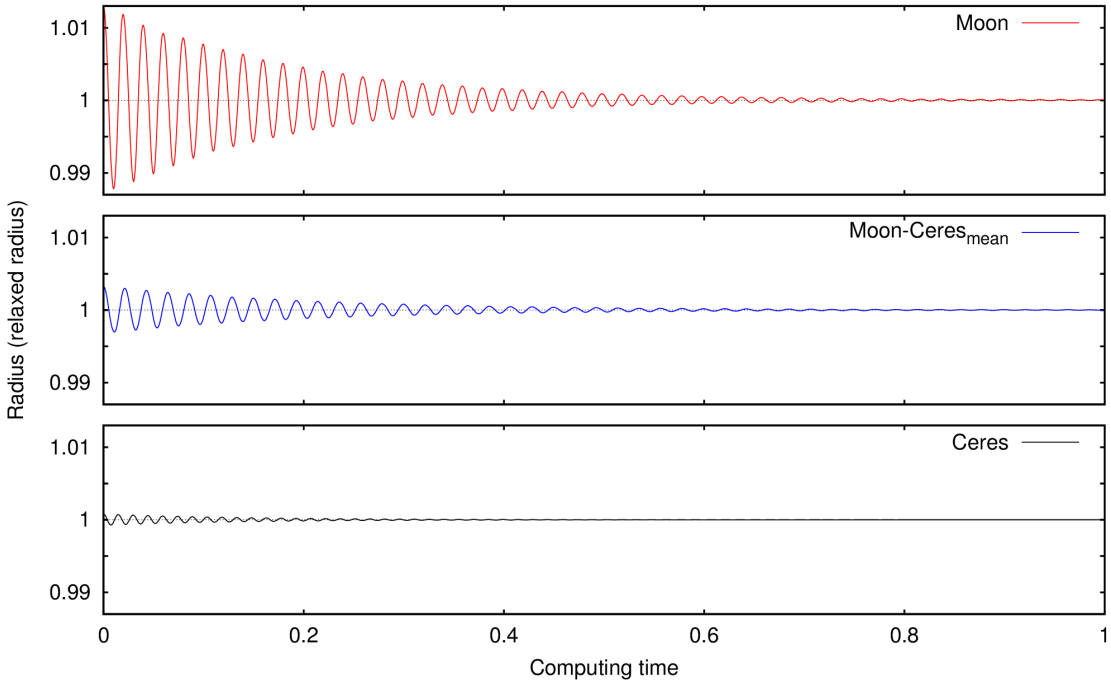

Figure 7 Illustration of the radial oscillation patterns during numerical relaxation for bodies with masses of the Moon (top), the geometric mean of the Moon and Ceres (middle) and Ceres (bottom). On the y-axis the outermost layer's radial distance is plotted, in units of the respective body's (final) radius. The computing time (x-axis) is normalized to an arbitrary unit for easy comparison. The strongly increasing oscillation strength with mass is immediately apparent and indicates a generally longer required computing time for more massive bodies. A more quantitative analysis confirms this behavior. All results related to these scenarios are provided in *Tab. 1*. A detailed discussion of them can be found there and in the text.

(output) time step[10]. However, because of the greater intensity of the ongoing dynamics with increasing mass, there is a clear trend towards a greater number of required integrator steps (for achieving the same relative accuracy), resulting in generally longer computing times for more massive bodies.

Besides measuring the exponential decay time, an *acceleration timescale* (τ_a), defined as the (computing) time necessary for the radial acceleration to drop below a certain (absolute) threshold value, is used. Since this acceleration indicates the forces (per unit mass) of the non-equilibrium oscillation, this can be considered a suitable measure for the achieved level of relaxation. In principle it can be obtained by a simple double differentiation of the radial oscillation function, like e.g. given in *Fig. 7*. The values given in *Tab. 1* all refer to an acceleration threshold value of $10^{-2}\,\mathrm{g}$ ($= 0.098\,\mathrm{m/s^2}$). While for the lowest-mass scenario this value is found already at the very beginning of the relaxation procedure, a strong trend towards computing time increasing with mass

[10]Since the number of integrator steps per time step is usually small, this can lead to rather discrete jumps in the required computing time when continuously increasing or decreasing the body's mass, even though the global picture is of course monotonic.

Scenario	Mass (kg)	Initial oscillation amplitude (radius)	Relaxed radius (km)	τ_d	τ_a
Ceres/10	9.43×10^{19}	0.00016	231	0.142	n.A.
Ceres	9.43×10^{20}	0.00075	498	0.140	0.13
Moon-Ceres$_{mean}$	8.33×10^{21}	0.0032	1027	0.217	0.4
Moon	7.35×10^{22}	0.013	2102	0.193	0.45
10×Moon	7.35×10^{23}	0.049	4398	0.19	0.67

Table 1 Summary of the scenarios considered for numerical relaxation, where each of the simulated bodies consists of a basalt core and an ice mass fraction of 0.25 in an outer shell. The initial oscillation amplitude is given in terms of the relaxed/final radius, which is also stated. Two different timescales are given for assessing the required computing time for relaxation (in arbitrary units), indicating the oscillation's exponential decay time (τ_d) and the elapsed time until falling below a certain absolute radial acceleration threshold (τ_a). Refer to the text for a detailed discussion. The three middle scenarios were investigated closer, where a depiction of their oscillation behavior is shown in *Fig. 7* (with identical units for computing time), and their respective final internal structure can be found in *Fig. 8*.

is found throughout the other scenarios, validating previous results. Depending on the relevant criteria a relaxed state has to fulfil, there are considerably longer computing times to anticipate for increasing masses.

To ensure comparability all computations presented in this section were carried out on the same machine, using the same basic parameters and utilizing the full solid-body physics SPH scheme, as presented in section 2. In order to reduce the amount of required computing time for numerical relaxation, one possible approach would be to significantly increase the (artificial) viscosity. However, this was not applied here, meaning that all presented computations were carried out with the same viscosity parameters that would be used in a subsequent actual simulation run. On the one hand it can be expected that the general trend of relaxation time increasing with mass remains, and on the other hand it was found that increased viscosity also results in a demand for smaller timesteps, which puts the expectation of shorter relaxation times (by stronger dampening) into perspective (Riecker, 2014).

Finally, another important issue – besides the required computing time – are the properties of the emerged internal structure. From the three important structural quantities density, pressure and internal energy, two – the pressure and the internal energy – are plotted in *Fig. 8*, representing the final, numerically relaxed state. The three graphs correspond to the same scenarios as in *Fig. 7*, which are in turn the three middle scenarios in *Tab. 1*. Even though the global shape fits the expected picture, strong distortions are immediately apparent, especially in the outer parts of the bodies. A closer look reveals them to be located at material boundaries, being the core-shell boundary and the transition from the shell to the surroundings in these cases. Owing to its size and therefore dominating the plots, the effects are particularly visible in the Moon-mass scenario, al-

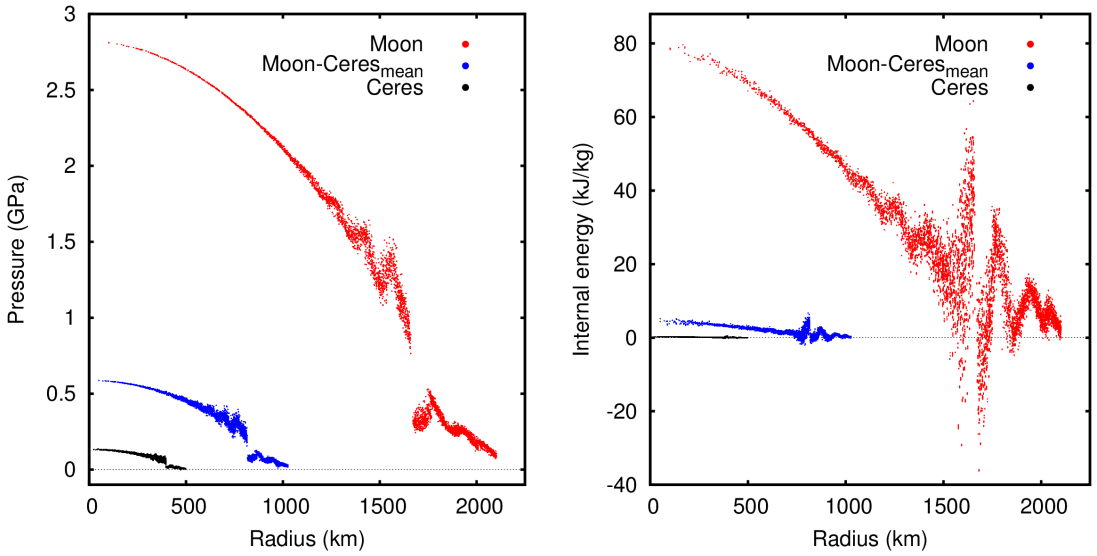

Figure 8 Internal structures resulting from numerical relaxation for the three middle scenarios in *Tab. 1* (see also *Fig. 7*, with identical color coding). The plots show the pressure (left) and the internal energy distribution (right) versus radius. Note the strong deviations at material boundaries, particularly in the internal energy structure (see the text for details).

beit present in the other two as well. Even though these structures of course represent equilibrium configurations, the demand for resemblance of reality is met only partly. Clear deviations from the expected monotone trend are found for both quantities, while they seem stronger pronounced for the internal energy distribution. Even large negative values occur, representing actually expanded, not compressed regions.

Summarizing, it can be said that in principle the numerical relaxation approach works good and is capable of eventually producing an ideally equilibrated configuration, but there are a couple of considerable drawbacks as well. Utilizing this procedure means to run the simulation program for a significant amount of time, just for obtaining the initial state, which in turn will then be the starting point of the actual simulation, thus valuable computing time has to be spared without contributing to the simulation run itself. Numerical experiments indicate that the amount of computing time required to end up with equally relaxed configurations increases significantly with the body's masses. This has to be considered in light of the fact that a suitable relaxation method generally becomes more important for more massive bodies. Another potential problem is that this method produces structures which are the final product of a giant damped oscillation history, which never happens in reality. This causes strong boundary effects and has particular influence especially on the internal energy distribution, representing the oscillation's dissipated energy. A further discussion of problems related to the numerical relaxation technique can also be found in section 3.2.3.

3.2.2 Semi-analytical approach

In section 3.2.1 the widely-used and relatively straightforward method of numerical relaxation was presented and discussed. In order to avoid – or at least minimize – its considerable drawbacks an alternative approach shall be elaborated here. The basic idea of this so-called *semi-analytical* relaxation is to directly solve the hydrostatic equations governing the internal structure of a spherical body in equilibrium, and to subsequently use the calculated distribution for producing a relaxed outcome by simply adjusting particle characteristics accordingly. While the numerical approach relies on simulating a damped oscillation until a final equilibrium state is reached, this method provides a more direct influence on the internal structure, allowing to closer resemble reality. In addition, even though the hydrostatic structure has to be calculated numerically (and is ultimately found only by an iterative approach), the required computing time turns out to be practically negligible.

The next paragraphs give an overview of the semi-analytical approach, by first depicting the calculation of the hydrostatic structure, before the treatment of the internal energy is explained and finally the practical implementation of the procedure is illustrated. To be able to discuss the problem not only from a theoretical point of view, certain practical approaches are chosen and explained in this section, in order to exemplify possible solutions to the given tasks. Not all of these solutions are necessarily intended to represent the most efficient or elegant possibility, but are sometimes chosen rather for the sake of convenience or simplicity as well.

Calculation of the hydrostatic structure

Looking at the given problem, the production of a relaxed spherical particle distribution, it almost suggests itself to look beyond the mere *brute force* numerical approach and to attempt examining the underlying, relatively simple, physics analytically. This continuum mechanics[11] picture should in turn be reproduced by the applied SPH algorithm, at least in the limit of high particle numbers, hence ensuring self-consistency. For the given geometry, i.e. spherical symmetry here, the continuum mechanics problem reduces to simple hydrostatics, even if the full solid mechanics treatment is considered in principle. In the following the set of equations determining the structure of a hydrostatic sphere is considered, aiming for a self-consistent solution thereof.

The fundamental starting point is inwards directed gravity balanced by a pressure gradient, expressed as

$$\frac{dp(r)}{dr} = -\rho(r)\, g(r) \quad , \tag{47}$$

with $g(r) = |\vec{g}(r)|$. This expression can be easily derived by considering gravity and pressure acting on an infinitesimally thin concentric shell (or a section thereof), with boundaries at r and $r + dr$ respectively. For the assumed spherical symmetry gravity (i.e. gravitational acceleration g) can be expressed simply as

$$g(r) = \frac{G\, m(r)}{r^2} \quad , \tag{48}$$

[11] The term *continuum mechanics* is commonly understood as an umbrella term for fluid mechanics and solid mechanics.

with the integrated mass $m(r)$ being all mass enclosed inside a radius r. Inserting (48) into (47), and adding an equation representing conservation of mass, results in the *Euler*[12] representation of the set of differential equations necessary for describing a spherical, hydrostatic configuration:

$$\begin{aligned} \frac{dp(r)}{dr} &= -\frac{G\,\rho(r)\,m(r)}{r^2} \\ \frac{dm(r)}{dr} &= 4\pi\,r^2\,\rho(r) \end{aligned} \tag{49}$$

With the pressure p and density ρ, all functions of the radial coordinate r, and the gravitational constant G, these equations represent conservation of momentum and mass, respectively. Another possibility to arrive at this representation of the momentum equation would be to directly utilize the hydrodynamic equation of motion (commonly referred to as *Euler equation*), like given in section 2.4 in (15). Requiring acceleration to vanish therein immediately results in the first equation in (49). An equation of state, connecting the thermodynamical quantities p, ρ and e along with a convenient treatment of the internal energy

$$\begin{aligned} p &= p\,(\rho, e) \\ e &= e\,(\rho) \end{aligned} \tag{50}$$

close, in principle, the system of equations for $p(r)$, $\rho(r)$, $m(r)$ and $e(r)$. The precise treatment of the internal energy is basically open to many different approaches. Here its final value is calculated for a given state of compression, neglecting non-mechanical contributions. Thus the internal energy can be determined for any given density (as a consequence of the level of compression) as indicated in (50). The next paragraph gives a detailed description of this procedure.

Basically it would be possible to use (49) and (50) along with an adapted version of the iterative apporach described below to calculate a body's hydrostatic structure, but transforming the equations into their *Lagrangian form*[13] makes life a lot easier. The transformation of (49) is trivial – forming the reciprocal of the equation for conservation of mass already yields the required result for this one. It can then be used again to transform the momentum equation by simple multiplication. Finally one ends up with the Lagrangian equivalent of (49),

$$\begin{aligned} \frac{dr(m)}{dm} &= \frac{1}{4\pi\,r(m)^2\,\rho(m)} \\ \frac{dp(m)}{dm} &= -\frac{G\,m}{4\pi\,r(m)^4} \end{aligned} \quad , \tag{51}$$

with all quantities – including the radial coordinate r of course – being now functions of the (new) independent variable m. Completing this system with the chosen equation of state poses a significantly greater challenge. Since (51) are differential equations for

[12] In this context *Eulerian description* usually refers to quantities depending on the radial coordinate r, instead of e.g. using some comoving coordinates (compare to the Lagrangian description below).

[13] This means to use the integrated mass m as the independent variable instead of r, therefore switching to a comoving coordinate system (compare to the Eulerian description above).

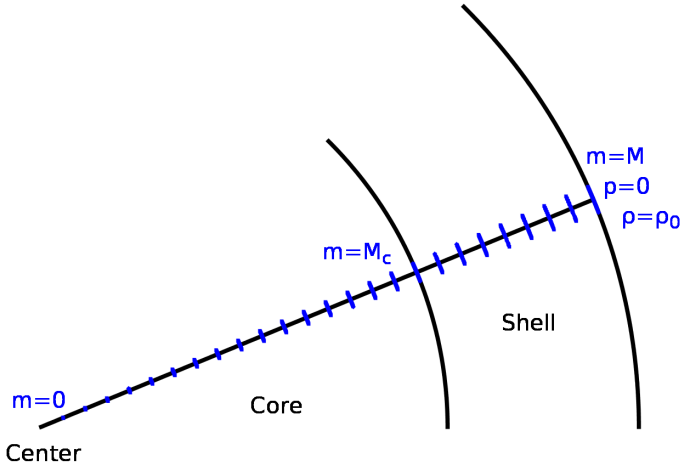

Figure 9 Schematic illustration of a spherical body with a given core-shell configuration. Typical boundary conditions for solving the hydrostatic equations – initially known only at the outer boundary – and discretization in the integrated mass m are depicted.

r and p, respectively, it is necessary to calculate the density for a given pressure (and internal energy), in order to be able to compute ρ as well, each time the numerical solution is advanced by one step (in m). This can be achieved by inverting the equation of state, usually given as $p = p\,(\rho, e)$, to obtain a function of the form $\rho = \rho\,(p, e)$. This should in principle be possible as long as the equation of state is bijective, even though it might not be possible to invert it analytically. To eventually conclude, the calculation of the internal energy, as already introduced in (50), can be inserted to end up with a so-called self-consistency problem, i.e. $\rho = \rho\,\big(p,\, e(\rho)\big)$. Solving this problem means to find (for a given p) the particular density which, once inserted on the right-hand side, is again obtained on the left-hand side. One possible approach for solving problems of this kind is to use a simple iterative procedure. Summarized, we find the following steps to end up with the iterative solution of the self-consistency problem for the density:

$$p = p(\rho,\, e) \quad \longrightarrow \quad \rho = \rho(p,\, e) = \rho\big(p,\, e(\rho)\,\big) \quad \longrightarrow \quad \rho^{(n+1)} = \rho\big(p,\, e(\rho^{(n)})\,\big) \quad . \tag{52}$$

Collecting the pieces together finally enables us to calculate $\rho(m)$, $p(m)$ and $r(m)$ from the differential equations (51) and from the iteration (52). The internal energy $e(m) = e\big(\rho(m)\big)$ can then be easily determined subsequently to complete the calculation of the hydrostatic structure.

How this can be carried out successfully in practice can be understood with the aid of *Fig. 9*, depicting a spherical body consisting of a core and a shell. The discretisation in m is schematically illustrated by blue tics. It is immediately clear that the numerical integration has to start at the outer boundary and be advanced inwards, since initially the properties at and around the center are entirely unknown, while conditions at the outer boundary are specified by the overall mass M, a given surface pressure, typically $p = 0$, and the surface density, typically the uncompressed density ρ_0 of the shell material. Due to the lack of knowledge of the body's radius (R) a suitable initial *guess* has to be

specified, being used as the starting point for the first inwards integration down to the core, i.e. from $m = M$ until $m = 0$. This initial uncertainty in R raises the necessity for an iterative approach, improving R with every iteration. This is repeated until the solution eventually converges towards a consistent internal structure, meaning $r(m = 0) \cong 0$ in particular. More details on practical realization and the iterative procedure are provided in the paragraph on implementation below.

Choosing the Lagrangian formulation of the hydrostatic equations has several major advantages concerning the numerical integration procedure, while the equations don't become significantly more complicated. Contrary to the final radius of the body, its mass is typically already known prior to the structure calculation[14], thus a well-defined domain of m-values is already available initially. This simplifies numerical integration, not least because boundaries (e.g. core-shell), typically also defined via enclosed mass, can be treated precisely. In addition, if (49) were used instead of (51), i.e. by integrating over r, not m, several problems can occur because of the initially not known overall range of r-values. One example would be a too large R, resulting in negative $m(r)$ towards the body's center (cf. (49)), which could in turn lead to negative pressures, causing serious problems with the equation of state. Using (51) on the contrary, rules out negative p because it is strictly monotonic increasing in the inwards direction, since m remains strictly positive. Hence the Lagrangian formulation of the problem has big advantages when it comes to numerical stability.

Treatment of the internal energy

As already indicated above, incorporating the internal energy into the framework of the hydrostatic equations requires some special attention. In principle the internal energy includes mechanical as well as thermal contributions. However, the treatment here considers only the mechanical parts, i.e. energy stored by compression of material, while neglecting thermal contributions. For the derivations in the last paragraph and throughout the rest of this work (whenever using the semi-analytical relaxation approach) the (specific) internal energy e is thus always determined according to $e = e(\rho)$, meaning a dependence on the density alone, indicating the current level of compression.

For actually calculating and setting e in the initial state of the simulation, the equation for conservation of energy (30) is drawn upon. Considering only the mechanical terms, the temporal evolution of the specific internal energy reads

$$\frac{de}{dt} = -\frac{p}{\rho}\,\mathrm{div}(\vec{v}) \quad , \tag{53}$$

with $\vec{v}$ being the flow's velocity, where a converging flow (compression, $\mathrm{div}(\vec{v}) < 0$) results in an increase of e, while the opposite (expansion) would result in a decrease. The idea is now to integrate this equation to finally obtain e for a given physical state (density) of the material under consideration. The basic assumption in the following steps is a homogeneous density and internal energy in a sufficiently big volume surrounding the point under consideration (where e is to be calculated), for every arbitrary but fixed instant of time. This basically means that a *homogeneous compression* is considered,

[14] However, this actually depends on the choice of input parameters which are – usually, but not necessarily – the desired masses of the bodies instead of their radii.

for all material inside the contemplated (sufficiently big) volume. Using this assumption the substantial derivative in (53),

$$\frac{de}{dt} = \frac{\partial e}{\partial t} + \vec{v}\,\mathrm{grad}(e) \quad , \tag{54}$$

reduces to $\partial e/\partial t$, since the gradient vanishes. Assuming in addition a constant (volume-) flow towards the considered point[15], to be more precise $-\mathrm{div}(\vec{v}) = \text{const.} = \alpha$, leads to an adapted version of (53):

$$\frac{\partial e}{\partial t} = \alpha \frac{p}{\rho} \quad . \tag{55}$$

The next crucial step is to invoke the continuity equation,

$$\frac{\partial \rho}{\partial t} + \mathrm{div}(\rho\vec{v}) = 0 \quad . \tag{56}$$

Differentiating the divergence by means of the product rule ($\mathrm{div}(\rho\vec{v}) = \vec{v}\,\mathrm{grad}(\rho) + \rho\,\mathrm{div}(\vec{v})$) allows to neglect the density gradient due to the above assumption. The final form of the continuity equation is thus

$$\frac{\partial \rho}{\partial t} = \alpha\,\rho \quad , \tag{57}$$

a simple ordinary differential equation with the solution

$$\rho(t) = \rho_0\, e^{\alpha t} \quad , \tag{58}$$

where ρ_0 represents the uncompressed density (i.e. the density for $p = 0$). This result simply describes the development of the density for homogeneous compression and a given α, which determines the (constant) volume flow into the considered region.

Collecting the pieces together, i.e. inserting (58) into (55), and setting $\alpha = 1$ for simplicity, eventually leads to

$$\frac{\partial e}{\partial t} = \frac{p}{\rho_0}\, e^{-t} \quad . \tag{59}$$

With the aid of a chosen equation of state and the analytical result for $\rho(t)$ in (58), the pressure can finally be expressed as $p = p(\rho, e) = p\big(\rho(t), e\big)$. Inserting this into (59) it becomes an ordinary differential equation for the temporal evolution of the specific internal energy $e(t)$ under the above assumptions. To finally end up with the desired result $e(\rho)$, this equation can be numerically integrated, starting at $t = 0$, with $e(0) = 0$, where the final time t_{end} can be easily calculated by inverting (58) for the desired ρ, i.e. for exactly the state of compression the internal energy shall be calculated for. This results in the upper limit for integration of (59), namely

$$t_{\mathrm{end}} = \ln\left(\frac{\rho}{\rho_0}\right) \quad . \tag{60}$$

Thus it is straightforward to compute the (mechanical) internal energy for any given density by means of any numerical procedure for integrating ordinary differential equations that comes to mind.

[15] And of course also towards every point in the considered (sufficiently big) volume.

An illustration of calculated internal energy structures, along with similar plots for other quantities, can be seen in *Fig. 10* for several differently massive bodies. A possible next step of improvement could be to extend these considerations by adding a suitable model for the thermal contributions to internal energy, which would bring the results another significant step closer to reality.

Results of the semi-analytical approach

The idea behind the semi-analytical approach is to produce particle distributions following the theoretical hydrostatic equilibrium structure. Particularly three quantities, the density, the pressure and the internal energy, are important in this respect. *Figure 10* shows hydrostatic structure results (black solid curves) of these quantities for scenarios representing masses of Ceres, the Moon, and the (geometric) mean of the two, with 25 mass% of ice and a basalt core each (scenarios identical to those in section 3.2.1, see *Tab. 1*). In principle these results represent perfect equilibrium configurations, however, a SPH particle setup produced according to them is still subject to minor numerical effects, especially at material boundaries. In order to assess the *quality* of the equilibrium achieved by an initial configuration following these structures, they were fed into sufficiently long simulation runs, allowing for all numerical effects to eventually settle. These final structures are plotted along with the initially calculated ones in *Fig. 10*. It is clearly visible that the overall structure remains basically unaltered, except for some numerical variance and boundary effects, hence it already represented an almost equilibrium state initially. The results are roughly the same for all considered scenarios, with only slightly stronger effects towards smaller masses for pressure and internal energy, and towards larger masses for the density. The strongest deviations of the final structure from the initial one are found for the internal energy distribution, where it suggests itself that this is connected to the non-continuous nature of the hydrostatic structure, therefore enforcing boundary effects.

In summary these results show that the semi-analytical relaxation approach results in initial configurations that are generally very close to equilibrium (cf. *Fig. 12*). In addition the magnitude of numerical boundary effects shows no strong dependence on the body's mass. When dealing with bodies made of a single material, these deviations would further decrease due to the absence of (internal) boundaries.

Implementation of the semi-analytical approach

As already outlined above the problem of producing relaxed initial conditions is approached mainly in two steps. The first one is to calculate the physically correct hydrostatic structure of a given body of given shell composition and respective masses. As a second step the calculated structure has to be assigned to the SPH particles. *Figure 11* depicts a flowchart of the practical implementation of this procedure, where the crucial steps shall be elaborated on in the following. While some of them are rather constrained, various possibilities exist for others. For the clarity of presentation a focus on one particular solution is set here whenever necessary.

The procedure starts with reading (typically) the desired masses of all components (core/shell) as main input parameters. These are used to make educated guesses for

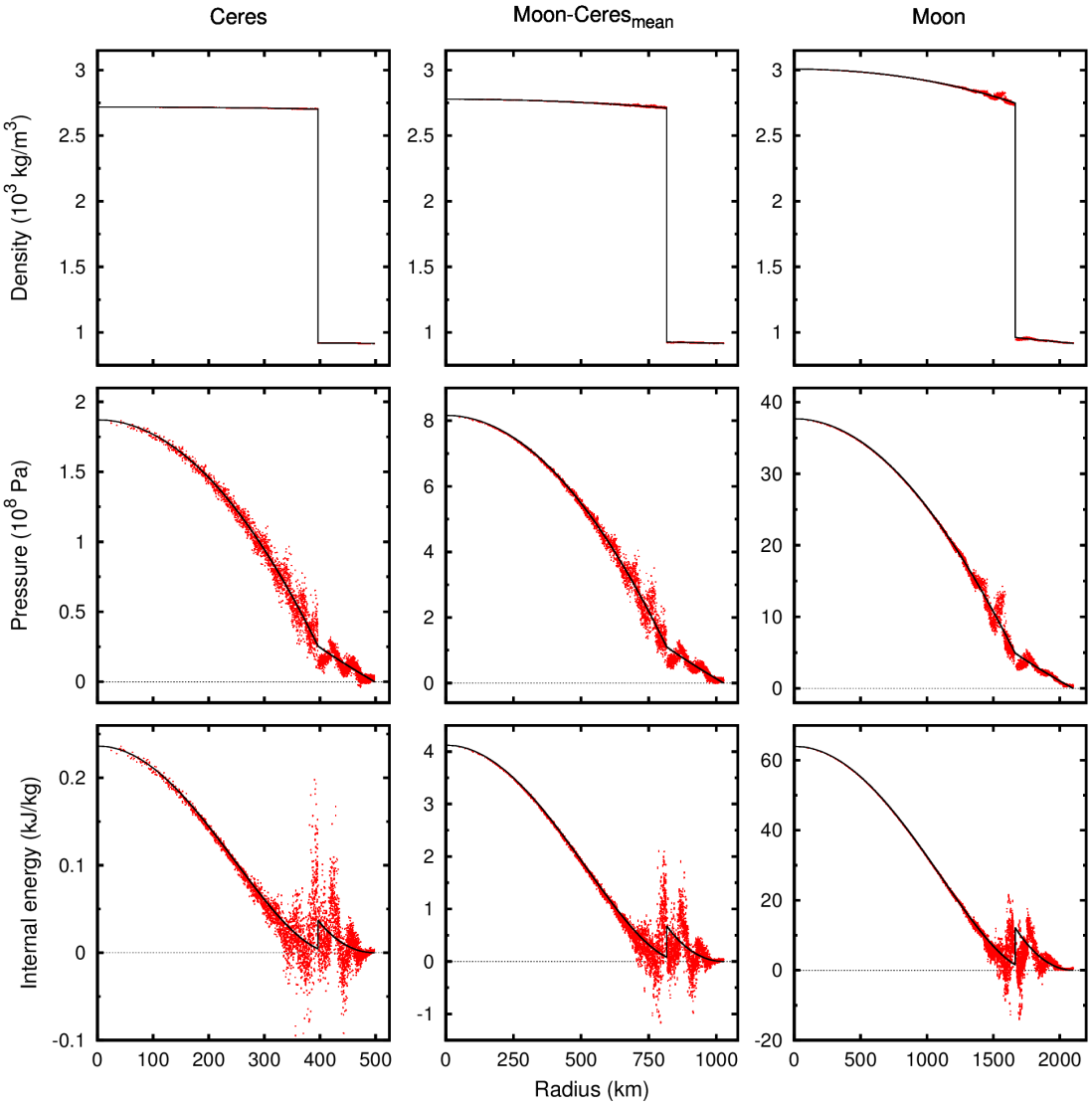

Figure 10 Comparison of calculated results for the hydrostatic structure (black solid lines) and their final appearance due to minor numerical effects after a sufficiently long simulation time (red). Each column represents one out of three different scenarios with masses of Ceres, the geometric mean of Ceres and the Moon and the Moon itself, all having a basalt core and 25 mass% ice in a shell. Note that the y-axis range is identical for the densities (first row), but considerably different for pressures and internal energies. See the text for a discussion.

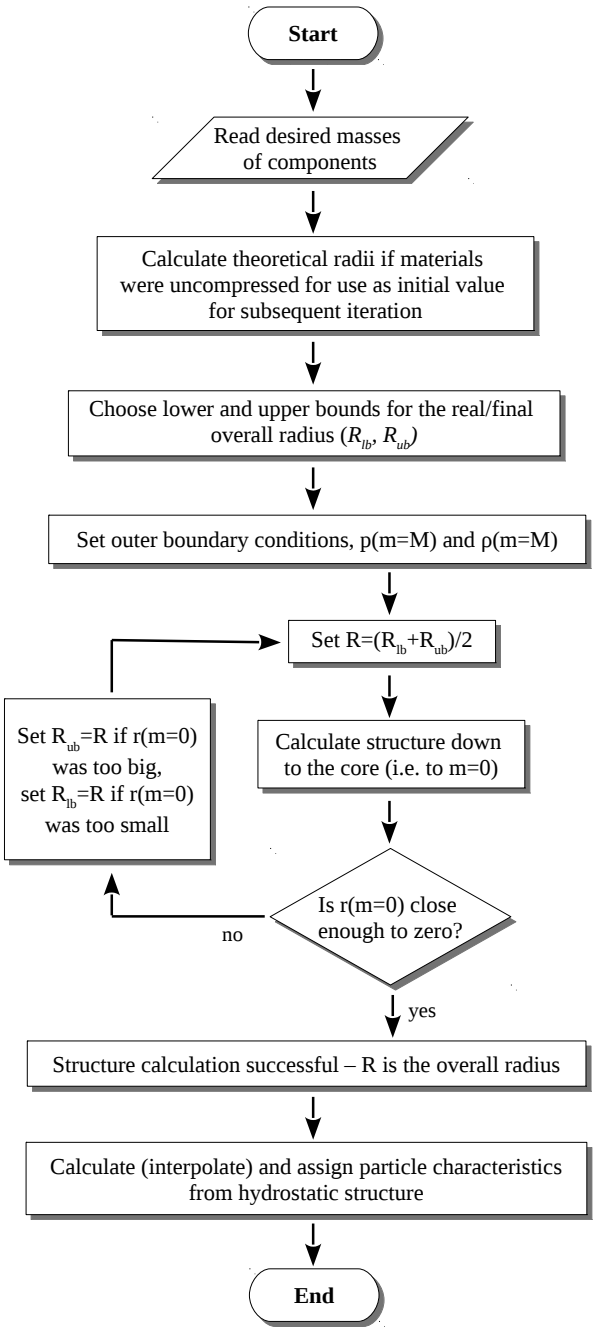

Figure 11 Flowchart of a possible implementation of the semi-analytical relaxation technique. See the text for further explanations.

the (initial) lower- and upper bound of the overall radius (R_{lb}, R_{ub}), making sure to definitely include its final value. Depending on the scenario details, they can for instance be deduced from the uncompressed (theoretical) radius of the body. After setting the outer boundary conditions, the iteration procedure starts and this interval is successively improved until the desired accuracy is achieved. *Figure 9* provides a graphical illustration of the integration domain, starting at the outer boundary and proceeding inwards to the body's center. The integration of (51) can in principle be carried out by any numerical scheme for ordinary differential equations. In addition (52) has to be iteratively solved for every numerical integration step. Like elaborated above the chosen equation of state has to be inverted for this, which is in principle possible as long as it is bijective, but it depends on its details how this can be carried out efficiently. As e.g. for the Tillotson equation of state (33), used for all simulations presented throughout this work, it is often necessary to resort to numerical means, since no analytical inverse can be found. In order to successively improve the overall radius (R) with every integration from the surface to the center (iteration), a simple choice is to follow a bisection-like method, which halves the interval $[R_{\mathrm{lb}}, R_{\mathrm{ub}}]$ with every further step (cf. *Fig. 11*). A good criterion to assess whether an assumed R (of a single iteration) was too small/big is to trace $r(m)$. Looking at the first equation in (51) shows that $r(m)$ is strictly monotonic decreasing in the inwards direction. This allows for testing the current R by means of the sign of $r(m=0)$, with a positive one indicating a too large R, and a negative one a too low value. Convergence of the iteration algorithm can then be defined as $r(m=0)$ falling into some small interval around zero, like e.g. $[0, R \times \epsilon]$, with a sufficiently small parameter ϵ. Once the desired accuracy is reached by hitting the respective interval for $r(m=0)$, the structure calculation can be considered successful, with (the last) R being the correct overall radius. The final step is to assign the calculated hydrostatic structure to the SPH particles, which can be achieved by simple interpolation, using any interpolation technique that comes to mind. However, linear interpolation might be sufficient, since the resolution (in m) of the structure calculation is usually relatively high.

The presented implementation represents probably not the most efficient way of performing the given task, with some methods being chosen for the sake of simplicity and clear presentation, rather than for pure performance. Improvements like extending the used simple Runge-Kutta 4 integrator, e.g. by adding adaptive stepsize control, could certainly enhance efficiency significantly. However, the whole described procedure can still be completed almost instantaneously, requiring maximum computing times of a few minutes on contemporary hardware. This depends slightly on various parameters, like the desired accuracy, and on the number of required iterations before convergence of course. Computing times of this magnitude can usually be entirely neglected when compared to typical times required for numerical relaxation or for the actual simulation run itself.

3.2.3 Numerical experiments

The last sections provided theoretical, but also practical insights into important problems and concepts of relaxation. These considerations shall now be brought together to gain a more comprehensive overview. The two main issues that will be treated in this section are a comparison of the numerical and the semi-analytical relaxation approach, along with a study on the basic relevance of relaxation focusing on the masses of the colliding

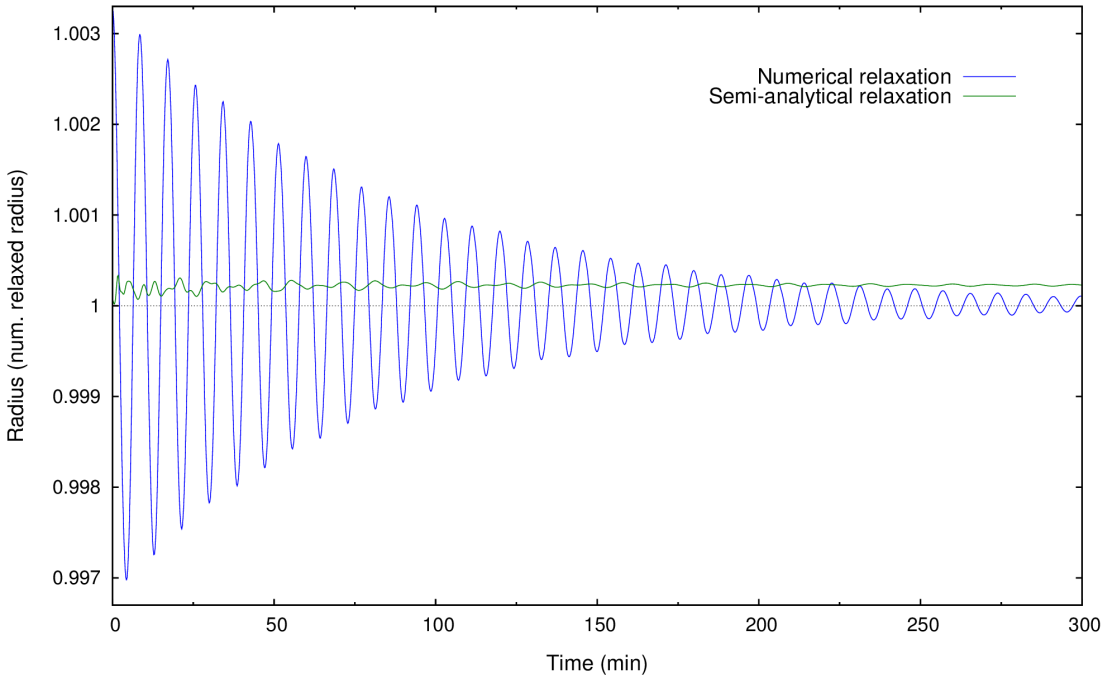

Figure 12 Comparison of the radial oscillation patterns during numerical relaxation (blue) and after semi-analytical relaxation (green) for a body with a 25 mass% ice shell and about 8.33×10^{21} kg, corresponding to the geometric mean of the Moon and Ceres (same scenario as already used above, cf. *Tab. 1*). The outermost layer's radial distance, in units of the numerical relaxation's final radius, is plotted over (physical) time. The obvious offset in y-direction is due to small differences in the production process of the scenarios' initial configurations, and is not important in this context. The scenarios are the same as the respective ones in *Fig. 7* and *Fig. 10*.

bodies as main parameters.

The results presented in *Fig. 10* already indicated that configurations produced by the semi-analytical approach are not entirely in equilibrium, but are still subject to some minor numerical effects. Even though the deviations from these somewhat *artificial* initial structures, emerging during the simulation run are small, it cannot be ruled out a priori that they have a significant influence on its outcome. A closer look reveals that the reason for these deviations are oscillation-like fluctuations, in principle comparable to those encountered at the numerical relaxation approach (cf. *Fig. 7*), but on a much smaller scale. Similar to those it is evident that these are not limited to the spatial coordinates but occur for other quantities (e.g. density, pressure, ...) as well, resulting in slightly disturbed distributions once the fluctuations have settled to an equilibrium configuration. This behavior is illustrated in *Fig. 12*, showing these small-scale oscillations for a body in the mass range between Ceres and the Moon (same scenario as in *Fig. 10*), where again the spatial coordinates were chosen. Along with that, the behavior of an equally composed, but initially unrelaxed body is plotted for comparison (same as in *Fig. 7*). The very large difference in magnitude is immediately apparent. In the following it will be shown that these remaining minor fluctuations have

no significant impact on the outcome of typical simulation runs by considering several general criteria, important for their overall result. These analyses were performed for four different, representative collision scenarios, each representing a certain mass range. To finally confirm that there is no significant difference between initial conditions produced by the semi-analytical approach and bodies initially in *perfect* equilibrium, each of these scenarios was independently computed four times, (1) initially unrelaxed, (2) semi-analytically relaxed, (3) numerically relaxed and (4) semi-analytically followed by numerically relaxed, resulting in an overall number of 16 simulation runs. The latter two on the list should indeed represent almost perfectly equilibrated configurations since the involved bodies were computed individually (prior to the actual simulation run) until no (significant) non-stationary fluctuations occurred anymore at all. (3) denotes the already introduced procedure of numerical relaxation (cf. section 3.2.1) and (4) combines both, setting up a particle distribution following the semi-analytically calculated internal structure, followed by an additional (brief) numerical relaxation to equilibrate the last remaining fluctuations (illustrated in *Fig. 12*). Expecting the semi-analytical approach being practically equivalent to *traditional* ways of setting up relaxed initial conditions (which would be (3) and (4) in the list above in this context) directly translates to expecting simulation outcomes to not deviate significantly from each other. However, defining what a *significant deviation* exactly is can be difficult when comparing *two* results. The choice of applying all methods (1) - (4) at once per collision scenario allows for a more sophisticated and reliable analysis, where the expectation now is that the results of the semi-analytical technique (2) are sufficiently close to the results of (3) and especially (4), particularly relative to outcomes of unrelaxed runs (1), whenever they deviate considerably.

The scenarios

The four chosen scenarios comprise grazing collisions above the escape velocity, leading to relatively strong interactions, but still followed by a clear separation of the (remaining parts of the) bodies after the actual time of contact. Representative snapshots, illustrating a typical scenario's development, are provided in *Fig. 13*. All scenarios feature a projectile-to-target mass ratio of approximately 1/10. The involved masses are similar to those already encountered above (see *Tab. 1*), with generally the same material composition – a basalt core and a shell made of water-ice – but with increased shell-mass fractions of 0.5 for the projectile and 0.25 for the target respectively. All simulation runs utilize a HCP lattice configuration and an initial relative rotation (cf. section 3.1) in order to minimize the influence of geometrical effects on the results. A total of approximately 50000 SPH particles was used in each computation. The precise values of all (relevant) collision parameters are summarized in *Tab. 2*, while *Fig. 14* illustrates the quantities' geometrical arrangement. From the total scenario masses it is evident that roughly 3 orders of magnitude are spanned, increasing to even 4 orders when the bodies' individual masses are considered (cf. *Tab. 1*), which is also a mass range of particular importance for planet formation (see e.g. Maindl and Dvorak, 2013). The impact velocities

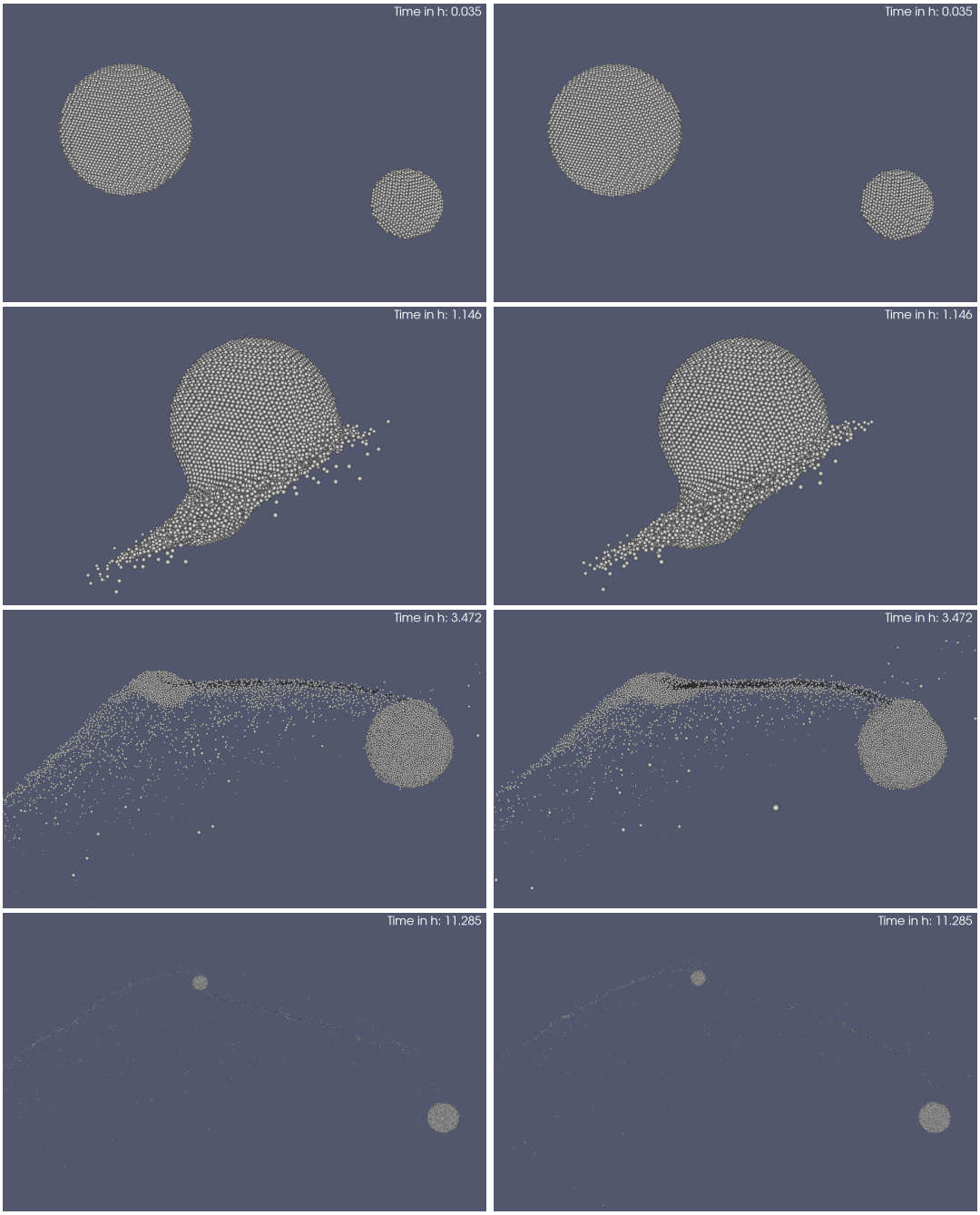

Figure 13 Simulation snapshots of the Moon-Ceres$_{mean}$+Ceres scenario (cf. *Tab. 2*) to illustrate the scenarios' typical development. Basalt and ice are color-coded in black and white. The left panels show a run with unrelaxed initial conditions vs. relaxed ones on the right, even though most differences are not clearly visible in this representation. A rather grazing collision is followed by a clear separation of the two main surviving bodies. Considerable amounts of material are transferred from the projectile (smaller body) to the target, before the material bridge dissolves. Simulation snapshots of the same scenario, but illustrating different physical aspects, are provided in *Fig. 16* and *Fig. 20*.

	Scenario		Total mass (kg)	v_{esc} (m/s)	v_0 (v_{esc})	α (°)
	Target	Projectile				
(a)	Ceres	Ceres/10	1.0373×10^{21}	418.2	1.691	38.8
(b)	Moon-Ceres$_{mean}$	Ceres	9.273×10^{21}	831.5	1.594	35.1
(c)	Moon	Moon-Ceres$_{mean}$	8.183×10^{22}	1789	1.494	36.7
(d)	10×Moon	Moon	8.085×10^{23}	3833	1.401	34.1

Table 2 Summary of the scenarios considered for the comparison of relaxation techniques and mass-dependent relaxation significance. All bodies have a basalt core and an ice shell with a mass fraction of 0.25 for the respective targets and 0.5 for the projectiles. The respective bodies' individual masses are identical to those in *Tab. 1*. v_{esc} denotes the two-body escape velocity at the time of first contact (see the text for details). The impact velocity v_0 and angle α are defined in the target's rest frame as depicted in *Fig. 14*. These quantities uniquely define the impact's principal geometry, while the bodies' radii would allow to calculate absolute positions, which is, however, not of particular interest here.

(as defined in the target's rest frame at the time of first contact[16], see *Fig. 14*) represent typical values for the chosen scenarios, as shown e.g. by Maindl and Dvorak (2013), well above the two-body escape velocity[17] and significantly increasing towards smaller masses involved. The general result of all considered scenarios is also in agreement with predictions on collision outcomes like provided by Leinhardt and Stewart (2012), who also include the projectile-to-target mass ratio as one of their investigated parameters. According to these results the range of impact velocities and angles considered here falls clearly into the *partial accretion* regime, being in line with the quantitative analyses in *Fig. 18* and *Fig. 19*, as well as with the (heuristic) impression from simulation snapshots (e.g. *Fig. 13*). Since each individual scenario is computed for four different relaxation states, there is of course some degree of variation in the precise geometrical arrangement at the time of collision. However, on the one hand these deviations are small, and on the other hand – more importantly – they originate from differences in the behavior of the initial relaxation states, which is exactly the subject of discussion. The precise geo-

[16] The smoothing properties of the SPH method make it in fact rather difficult to precisely define the *moment of first contact*, therefore the last timestep before non-gravitational interaction sets in – i.e. before the bodies' mutual distance falls below the smoothing length – is used here as a definition thereof.

[17] For two bodies – where neither of their masses is negligibly small – the mutual escape velocity is given by $v_{esc} = \sqrt{2\,G\,M/r}$ with the gravitational constant G, $M = m_1 + m_2$ and r being the masses' separation. Strictly speaking this holds only for point masses or for perfect spheres (which can be replaced by equal point masses without effects on their dynamics). For $m_1 \gg m_2$ the gravitational pull of m_2 on m_1 can be neglected and the problem reduces to a central force field (generated by m_1) acting on m_2 (a one-body problem) where the potential energy of m_2 can be readily expressed, and set equal to the kinetic energy for obtaining $v_{esc} = \sqrt{2\,G\,m_1/r}$, depending solely on m_1. But even in the general case the two-body problem can be reduced to an equal one-body problem for the masses' relative motion, with the reduced mass $\mu = m_1 m_2/(m_1 + m_2)$ orbiting a fixed (in space!) central mass $M = m_1 + m_2$. This formal central force field (generated by M, acting on μ) allows for directly expressing the potential energy of μ (w.r.t. this field, and hence w.r.t. M) for any separation. Equating this again to the kinetic energy finally allows for a straightforward calculation of the two-body escape velocity as stated before.

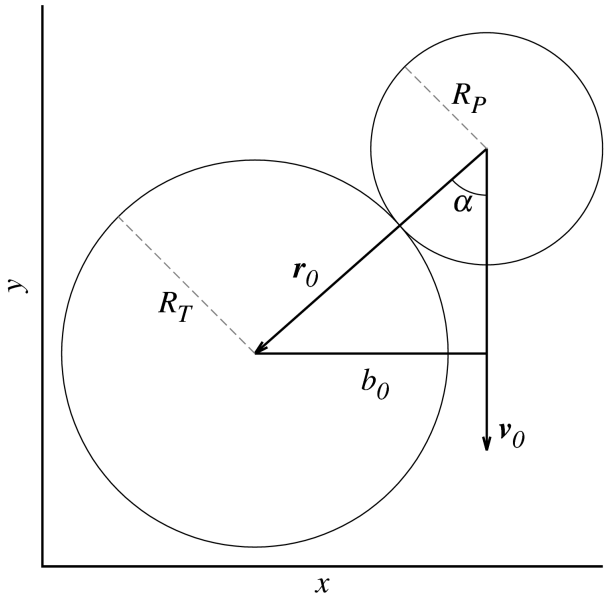

Figure 14 Collision geometry in the target's rest frame (lower left body), illustrating the moment of first contact (actually it is more complicated – see the text for details). The impact angle α, impact parameter b_0, impact velocity vector $\mathbf{v}_0$ and the relative vector from the projectile's center to the target's center $\mathbf{r}_0$ are labeled. The actual impact velocity (as stated e.g. in *Tab. 2*) is simply given by $v_0 = |\mathbf{v}_0|$. For given $\mathbf{v}_0$ and $\mathbf{r}_0$ the impact angle α can be calculated from the properties of the scalar product, with $\mathbf{r}_0\mathbf{v}_0 = |\mathbf{r}_0||\mathbf{v}_0|\cos(\alpha)$.

metrical arrangement at the very beginning of a scenario's individual simulation runs is *exactly* the same, with equal velocities and an initial distance of $3 \times (R_P + R_T)$, allowing for the build-up of possible tidal effects (using always – arbitrarily – the radii of the relaxed case (2)).

Summarizing it is evident that the chosen parameters represent quite typical giant collision scenarios, particularly concerning the impact velocities and angles, resulting in all cases in partial accretion of projectile material onto the target, followed by a clear separation of the remaining bodies towards the end of the simulated time span, allowing for an analysis of the then remaining fragments. The relatively high ice mass fractions additionally allow for clearly tracing transport and loss of volatiles.

Validation of the semi-analytical approach

In order to confirm the equality of the three considered relaxation approaches ((2) to (4) in the list above) and hence to validate the semi-analytical approach, the *evolution of the averaged damage* is considered as the first one out of four criteria. The respective plots for all scenarios in *Fig. 15* clearly indicate the time prior to the bodies' first contact, followed by a steep rise during the actual collision and an off-leveling in its aftermath. While the results for the semi-analytical approach lie well within the typical variance indicated by the differences of the two *perfectly* relaxed runs, there are considerable deviations for the unrelaxed cases for all scenarios. However, significantly increased damage

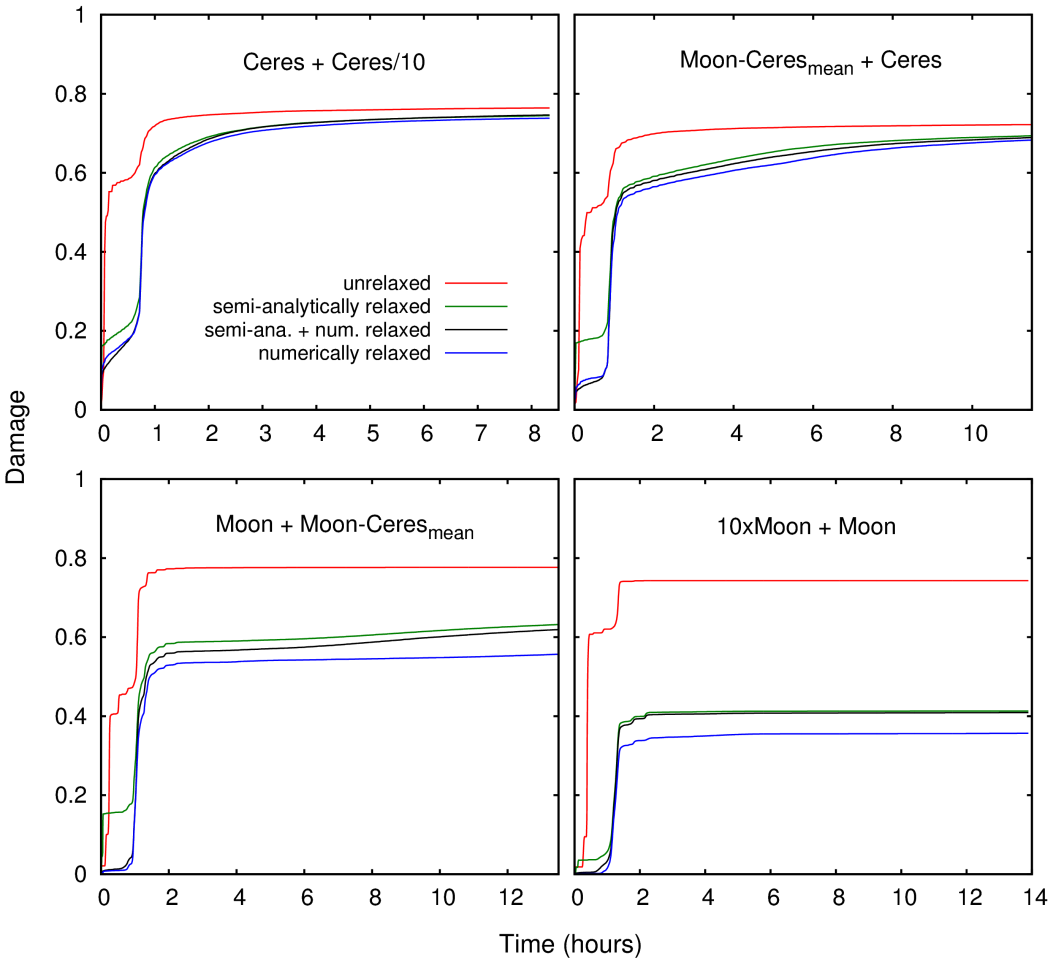

Figure 15 Evolution of the overall average damage for all considered scenarios and relaxation approaches. The time prior to the actual collision and the roughly constant level after it can be clearly distinguished. Simulation runs with relaxed initial conditions show a considerably different behavior compared to their unrelaxed counterparts. This effect even increases for higher masses involved.

levels during the time span before the collision event are found for the semi-analytical compared to the other two relaxation approaches. The reason are the aforementioned minor fluctuations which remain after setting the hydrostatic internal structure and lead to some non-physical damage at material boundaries (cf. *Fig. 16*). The further evolution however, indicates for all scenarios that this transient phenomenon does only insignificantly influence the development of the damage in the later stages after the collision.

The next criterion for comparison is the *evolution of the overall kinetic energy*, as shown in *Fig. 17*. Deviations in this quantity generally indicate differences in the state of motion of the involved bodies, i.e. in positions, velocities or rotation. An initial increase until the instant of first contact is followed by a steep decrease during and after the collision. The validity of the semi-analytical approach can be confirmed again – its results match the other two relaxation strategies, while deviating, relatively little but significantly, from the unrelaxed case, at least for some scenarios. Particularly clearly visible in the most massive scenarios are the strong oscillations associated with unrelaxed initial conditions.

Questions concerning the transport and loss of mass in general and of volatiles in particular, during such collision events, give rise to the last two considered criteria, *overall fragment masses* and the *fragments' ice masses*. The partial accretion type of simulations results in well-separated fragments after an interaction phase during the collision. Therefore it suggests itself to trace the masses of the two largest fragments as well as the combined mass of the rest of the material. The evolution in these three categories for all scenarios and relaxation states can be found in *Fig. 18* (overall) and *Fig. 19* (only ice). Except for some minor deviations, the semi-analytical results are again in good agreement with the other initially relaxed runs. Since these deviations are always of similar magnitude to typical differences between the two ideally relaxed runs they can be attributed to random effects rather than to systematic ones. The behavior of the unrelaxed runs on the contrary frequently differs significantly. This is particularly well visible in scenarios (b) and (c).

Mass dependence of relaxation relevance

After validating the semi-analytical approach, the same simulation scenarios shall now be used to investigate the relevance of actually applying a relaxation technique in the first place. The scenarios were chosen to be mainly identical except for the different mass-range represented by each of them. This allows to examine mass-dependent differences of relaxed vs. unrelaxed initial conditions, or in other words the necessity of applying a suitable method of relaxation depending on the colliding bodies' masses.

The investigation comprises the same four criteria already used before, illustrated in *Fig. 15* to *Fig. 19*. It was found above – and is evident from the figures – that the 3 different applied relaxation techniques yield basically equivalent results, thus in principle either of them can be considered for comparison with the unrelaxed results.

For the evolution of the average damage (*Fig. 15*) a clear trend towards differences increasing with the involved masses can be seen. Their highly increased damage levels originate in the strong initial oscillations of unrelaxed initial conditions (see *Fig. 16* for an illustration of the typical damage evolution). While the final level in the unrelaxed runs levels off at roughly the same value for all scenarios, final values in the relaxed cases decrease with increasing masses. The reason is probably the increasing gravitational

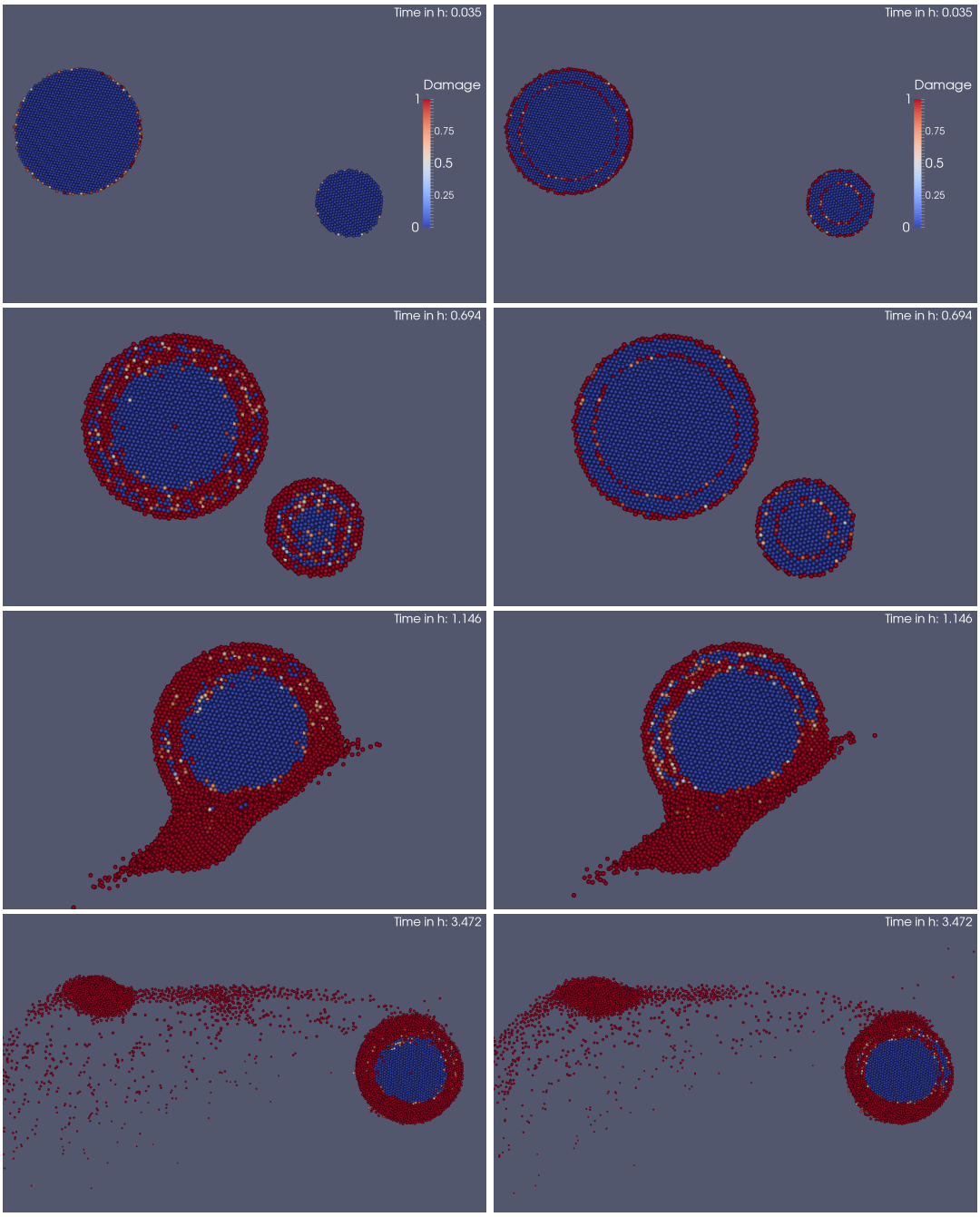

Figure 16 Simulation snapshots (actually cuts thereof to show the interior) of the Moon-Ceres$_{mean}$+Ceres scenario (cf. *Tab. 2*) to illustrate the scenarios' typical damage evolution. The left panels show a run with unrelaxed initial conditions vs. relaxed ones on the right. Boundary effects are visible prior to the collision for the (semi-analytically) relaxed scenario, leading to some (non-physical) damage. In the unrelaxed run on the contrary large amounts of damaged material appear already before first contact. These differences – albeit smaller – continue even after the actual collision to some degree. Simulation snapshots of the same scenario, but illustrating different physical aspects, are provided in *Fig. 13* and *Fig. 20*.

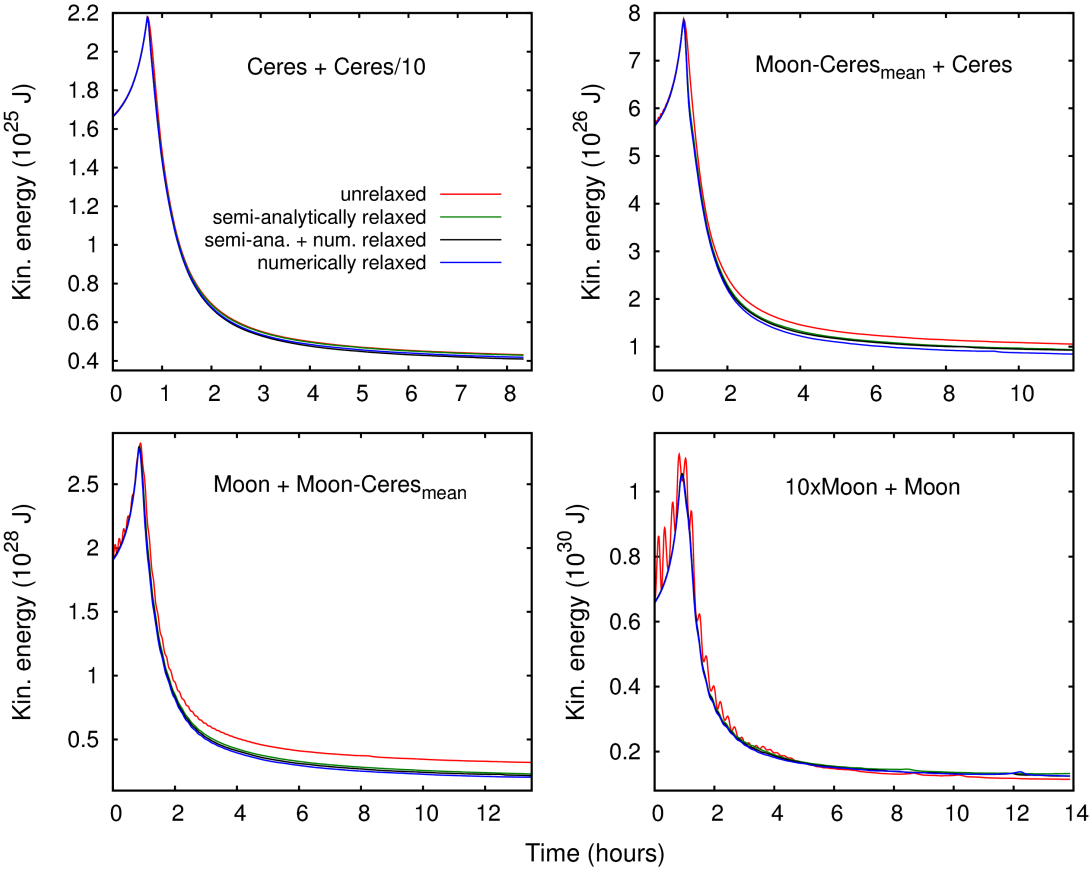

Figure 17 Evolution of the overall kinetic energy for all considered scenarios and relaxation approaches. An increase due to gravitational acceleration prior to the actual collision and a strong decay afterwards can be clearly distinguished. In most cases simulation runs with relaxed initial conditions show a considerably different behavior compared to their unrelaxed counterparts. Note the clearly visible oscillation patterns in the unrelaxed curves of the most massive scenarios.

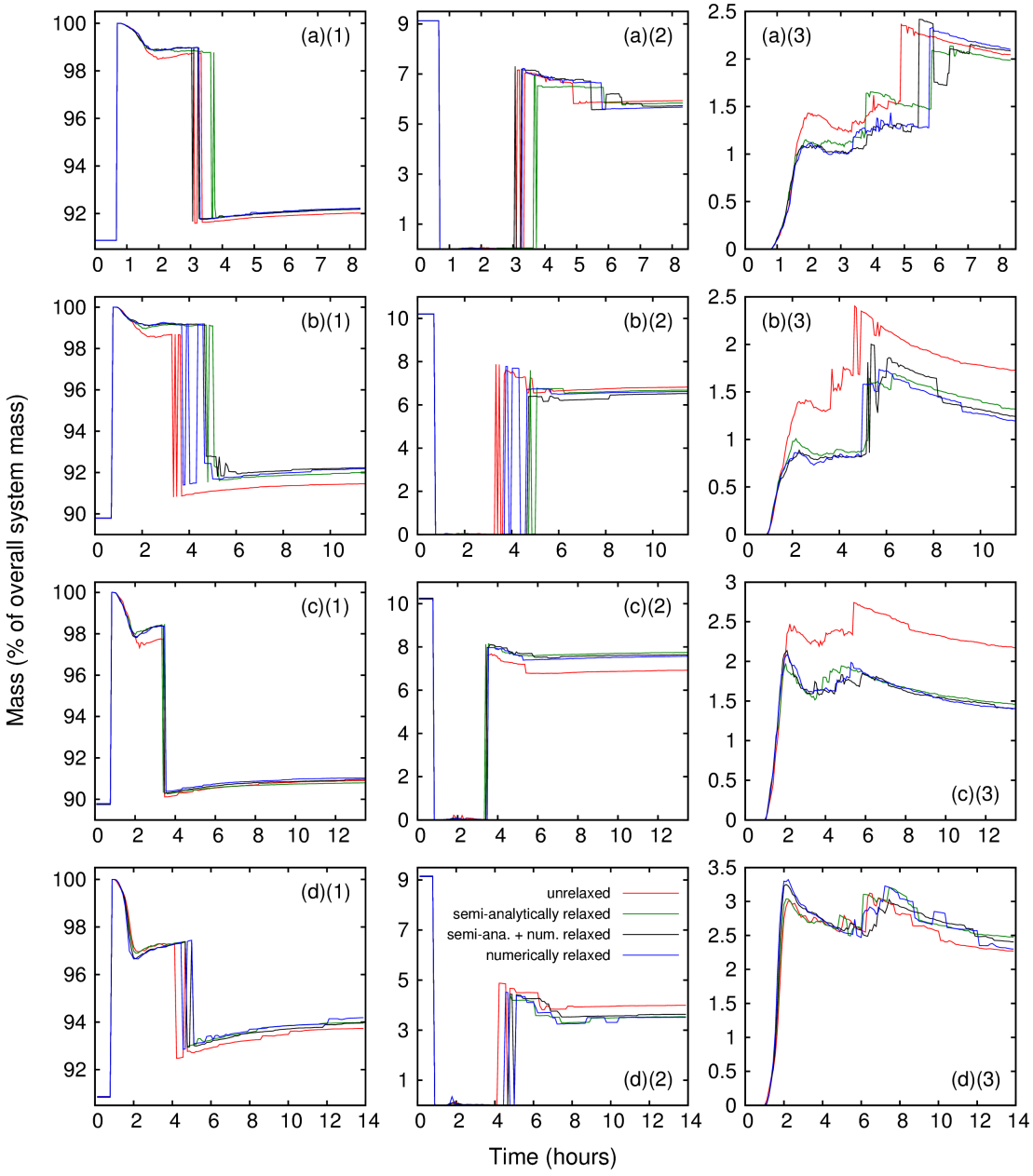

Figure 18 Evolution of the overall masses of the largest fragment (1), the second largest fragment (2) and the rest (3) for all considered scenarios ((a) - (d), see *Tab. 2*) and relaxation states. The partial accretion nature of the scenarios is best visible in the higher/lower masses after the collision in (1)/(2), compared to initial target/projectile masses. The semi-analytical results are always well within the range of the other two applied relaxation techniques, while the behavior of the unrelaxed runs frequently deviates significantly – particularly well visible in scenarios (b) and (c).

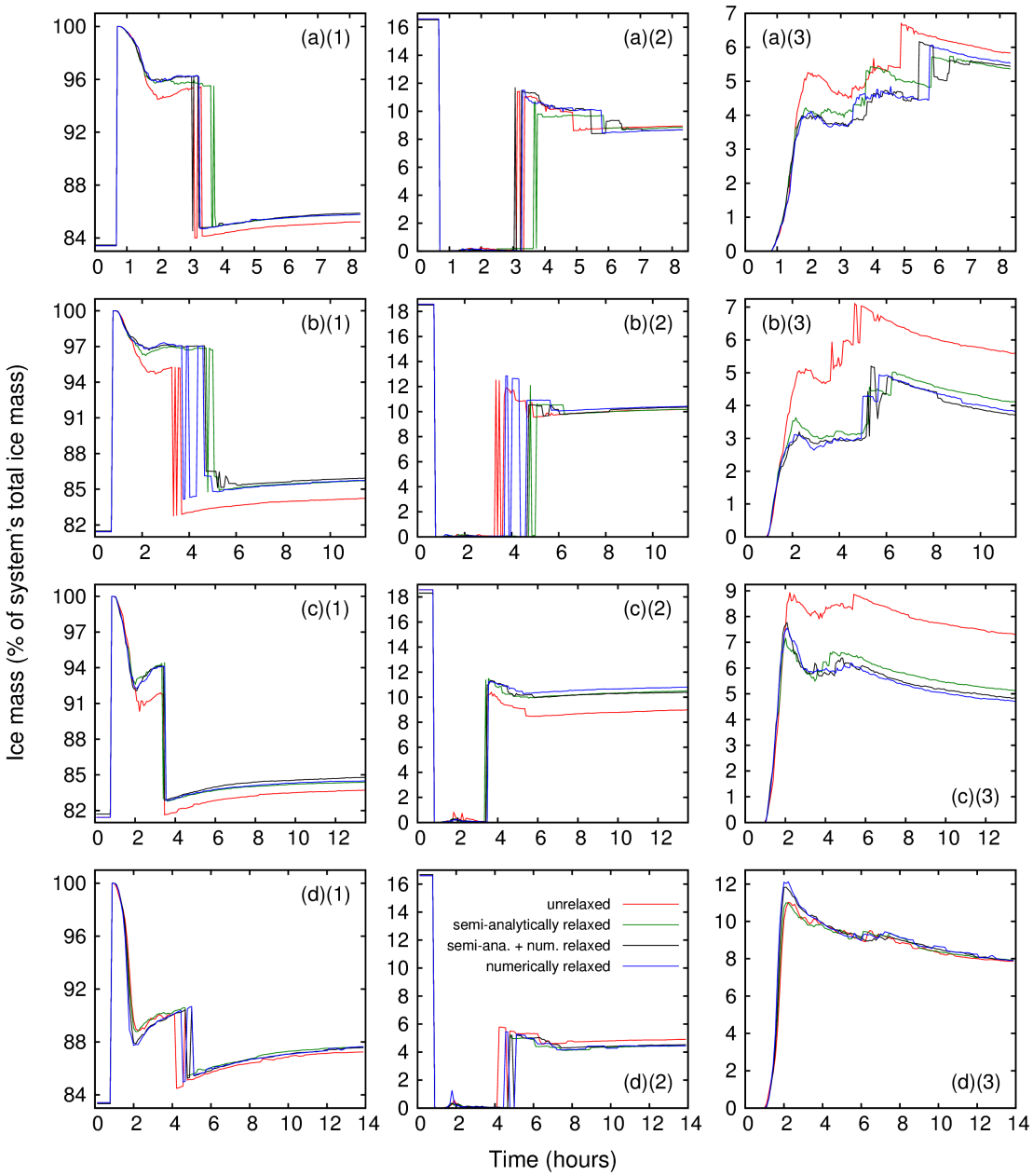

Figure 19 Evolution of the ice masses of the largest fragment (1), the second largest fragment (2) and the rest (3) for all considered scenarios ((a) - (d), see *Tab. 2*) and relaxation states. The semi-analytical results are always well within the range of the other two applied relaxation techniques, while the behavior of the unrelaxed runs frequently deviates significantly – particularly well visible in scenarios (b) and (c).

strength, which is able to bind the SPH particles more efficiently, counterbalancing tensile forces. Significantly different damage levels result in different material properties, due to loss of internal strength, resulting in material behaving rather like a fluid once it is (entirely) damaged in a certain region.

The development of the kinetic energy (*Fig. 17*) exhibits rather little differences between relaxed and unrelaxed simulation runs. However, deviations seem to slightly increase with mass, where the unrelaxed curve in the most-massive scenario is dominated by large-scale damped oscillation patterns. Differences in kinetic energy generally indicate different fragment velocities or rotation characteristics, possibly leading to a deviating dynamical evolution of a given scenario.

A rich variety of behavior can finally be found for the evolution of overall fragment masses (*Fig. 18*) and the fragment's ice masses (*Fig. 19*). For the most-massive fragment (panels (1), the target at the onset of the simulation run) reduced overall masses, as well as ice masses by up to a few percent are found in the unrelaxed cases, consistently throughout almost all scenarios. The second largest fragments (panels (2)) display a rather diverse behavior, where the Moon+Moon-Ceres$_{mean}$ scenario (c) features the biggest differences, with significantly larger amounts of material lost in the unrelaxed case. The by far largest differences are found for the rest of the material (panels (3)), especially in the intermediate mass scenarios (b) and (c). Computed with unrelaxed initial conditions, these scenarios show a mass increase of up to 50 percent compared to relaxed simulation runs. Therefore considerably more material – particularly ice – is lost as debris when using unrelaxed initial conditions. Some of the mentioned effects are also visible in *Fig. 20*. The final impression from analysing fragment masses and their ice contents is that differences seem to be most enhanced for intermediate mass bodies, ranging roughly between Ceres' mass and the Moon's. However, this trend is not very strong and the sample – consisting of the four scenarios – is rather small.

One of the main reason for the identified differences of unrelaxed and relaxed runs might be that damaged material shows different properties and behavior. This makes the unrelaxed runs' strong initial oscillations – responsible for the increased damage levels – one of the main contributors to the observed effects. In less damaged regions more energy is transferred into elastic loading during the collision, resulting in less available energy for accelerating material away from the main bodies. This is confirmed by the unrelaxed runs' increased levels of kinetic energy. Concerning the relevance of relaxation, no strong trend with mass was found, even though scenarios involving higher masses seem to be slightly more affected by the difference between relaxed and unrelaxed initial conditions. Although the considered scenarios represent rather typical partial accretion encounters, it is important to keep in mind that stronger or additional effects cannot be ruled out for sufficiently different scenarios. In order to avoid deviations like the above, applying a suitable relaxation technique is a necessity, at least for the considered range of masses, and probably also beyond.

3.3 Summary and conclusions

The choice of proper initial conditions for a subsequent SPH simulation is driven by optimizing characteristics like isotropy, particle noise and resemblance of reality. The demand for isotropy – of course at least only as long as a physically isotropic material is to be simulated – is closely related to (lattice-) symmetries in the initial configuration.

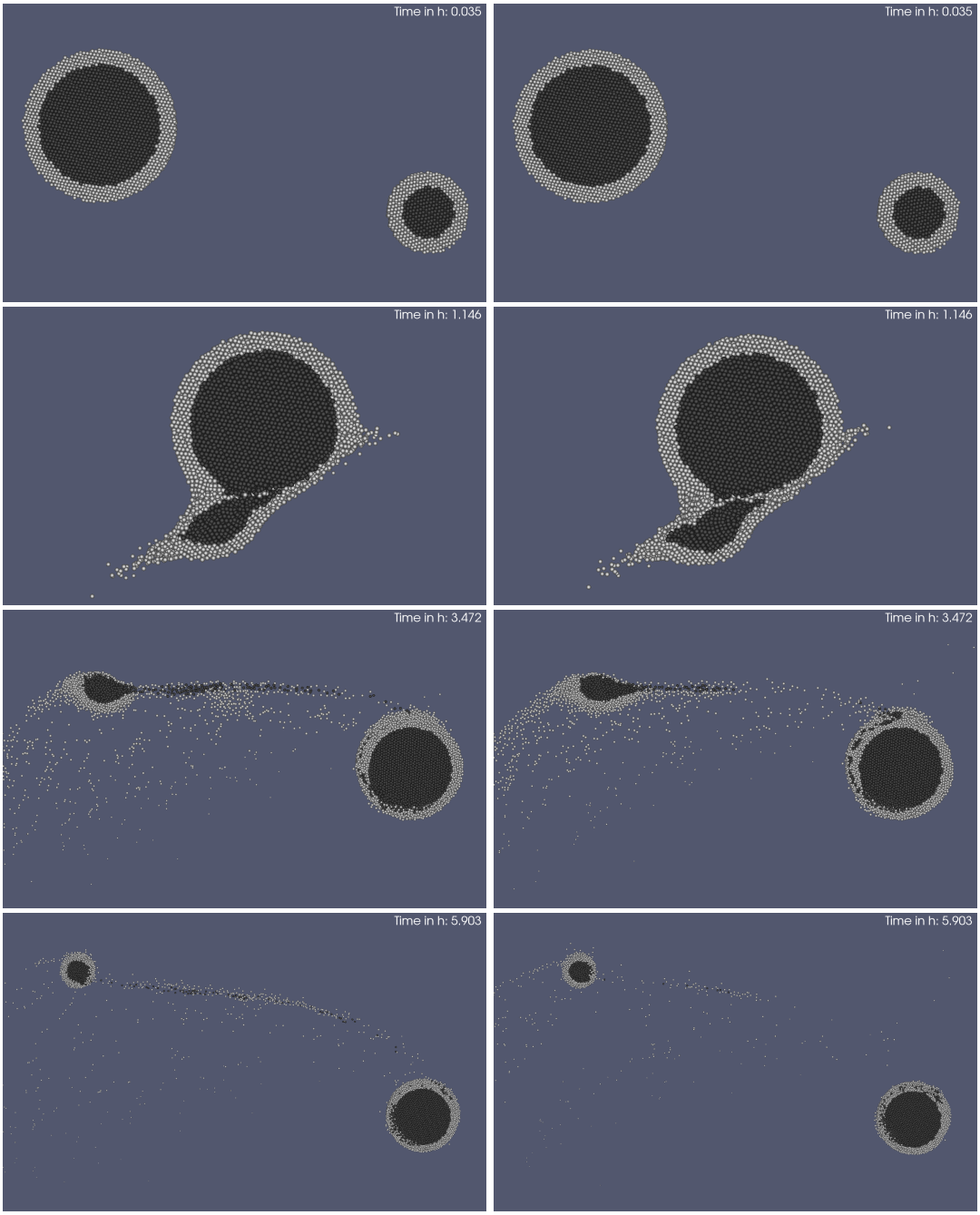

Figure 20 Simulation snapshots (actually cuts thereof to show the interior) of the Moon-Ceres$_{mean}$+Ceres scenario (cf. *Tab. 2*), illustrating the scenarios' typical distribution of material types. Basalt and ice are color-coded in black and white. The left panels show a run with unrelaxed initial conditions vs. relaxed ones on the right. The basic trend that the projectile (smaller body) is ripped apart and partly accreted onto the target is apparent for both runs, while the amounts of material transferred, its distribution and the amount lost to the surroundings differ significantly. Simulation snapshots of the same scenario, but illustrating different physical aspects, are provided in *Fig. 13* and *Fig. 16*.

The comparison of different lattice geometries, also considering initially slightly rotated bodies to further reduce symmetries, shows indeed clear differences in lattice effects, namely between SC and HCP lattice configurations. A strongly anisotropic behavior, apparent in particular in the global mass distribution, can be observed for the SC lattice, especially when compared to an (initially rotated) HCP particle setup, which shows significantly better characteristics in this respect.

Beyond geometrical issues, starting SPH simulation runs with (sufficiently) relaxed initial conditions is important in order to avoid undesired behavior as a result of an initial disequilibrium where none is supposed to be. A popular and straight-forward method is numerical relaxation, where an initial configuration that is not in equilibrium – like e.g. a homogeneous sphere – is simply put into the simulation program until it settles into a relaxed configuration. Albeit relatively simple, this method has the big disadvantage of consuming large amounts of valuable computing time, solely for producing the initial state of the actual simulation run. An analysis on the mass-dependence of the required computing time resulted in computational needs increasing with mass. Later it was shown that higher-mass scenarios tend to be prone to at least as much and perhaps stronger artifacts from unrelaxed initial conditions, which would mean that the necessity for relaxation also increases with mass. In order to overcome these drawbacks of the numerical relaxation technique, a different strategy is presented. Termed *semi-analytical relaxation*, the approach basically incorporates the calculation of a body's (theoretical) hydrostatic structure, and adjusting the SPH particles' properties accordingly. With computing times in the order of one minute, they can be considered negligibly small compared to timescales of typical simulation runs. The results produced with the semi-analytical approach were shown to be close to equilibrium configurations, even though some minor numerical effects remain. A further analysis, by comparing these results to long-time numerically relaxed initial conditions (which can thus be considered almost perfectly relaxed) finally validated the semi-analytical approach. This was done for four different collision scenarios, representing masses ranging from below Ceres' to above the Moon's, with the results of the semi-analytical approach matching virtually always those of its numerically relaxed counterparts. The criteria consulted for comparison include the evolution of fragment masses and the amount of material lost to the surroundings as debris, which is important in the context of questions related to planet formation, especially when it comes to materials of particular interest like water ice. The same scenarios and criteria were drawn upon again to investigate the relevance of relaxation in the first place, particularly w.r.t. the considered masses of the colliding bodies. It was found that significant differences between relaxed and unrelaxed simulation runs are present throughout all considered mass-ranges, possibly with a slight increase towards higher masses. They include larger amounts of material lost as debris as well as considerably differing damage values in the unrelaxed cases, to name but a few. The big differences in damage levels, and a material's different behavior related to it, might be one of the main reasons for the differences between relaxed and unrelaxed simulation runs.

Since the results are close to identical, the semi-analytical approach can be considered a real alternative to the more direct procedure of numerical relaxation. Besides saving valuable computing time by working almost instantaneously, the emerging internal structures can be controlled better and easier. However, as elaborated above the semi-analytically relaxed configurations are not entirely in equilibrium, and if one is interested

in getting rid of these minor remaining fluctuations as well, an additional numerical relaxation can be applied anytime. Compared to numerical relaxation *from scratch* the required computing time to produce equally equilibrated results is of course much lower in general. One example where such a strategy might be inevitable anyway are very massive bodies, where the (huge) initial oscillations of a sole numerical relaxation approach might lead to numerical problems and perhaps a crash of the simulation program itself. In practice the choice between numerical relaxation and the semi-analytical approach might also depend on the kind of simulations one is interested in. Considering the typical case of a parameter study as an example, the additional computational costs of numerical relaxation will be low if the colliding bodies themselves remain identical throughout many simulation runs (while other parameters like impact velocity, etc. are varied), but will be very high if they do not, demanding individual relaxation treatment of a large number of runs. In the first case the numerical relaxation procedure has to be computed only a few times (perhaps only once), while the second one could require numerical relaxation prior to each new simulation run, where the large amounts of saved computing time with the semi-analytical approach may easily outweigh the additional costs of its implementation. A good example can be readily found in this work, where the scenarios considered in the study in section 3.2.3 comprise different bodies (in mass and composition), resulting in potentially very high computational costs for numerical relaxation, in contrast to the semi-analytical approach.

Further research into these topics could include an extended mass range, and particularly an extension towards other basic types of collisions (apart from partial accretion). The rather small sample of four different scenarios in section 3.2.3 can clearly not account properly for the vast number of possible collision outcomes, but shall illustrate the mass-dependency of relaxation relevance exemplarily with a typical parameter setup. Another interesting question would be how much of these results still holds for purely hydrodynamical simulations, neglecting solid-body behavior, unlike in all simulations presented here. Since a substantial amount of the found differences between unrelaxed and relaxed runs might be attributed to different damage levels, it suggests itself that these differences may be significantly less pronounced without any incorporated damage model. Finally the particle number might influence the obtained results as well. If setting the hydrostatic structure produces in principle a perfect equilibrium (i.e. also in terms of the numerical SPH scheme), the remaining fluctuations and boundary effects of the semi-analytical approach can be expected to decrease with increasing particle number (and eventually vanish in the asymtotic limit $N \to \infty$).

Acknowledgements

First of all I would like to thank my supervising tutor *Professor Rudolf Dvorak* and my colleague *Thomas Maindl* from the *Institute of Astrophysics* in Vienna for their ongoing support and advice. In addition my gratitude goes to *Christoph Schäfer*, *Roland Speith* and *Janka Werner* from the *University of Tübingen* for many fruitful discussions and interesting and pleasant visits at their institute. This thesis was also partly funded by the FWF Austrian Science Fund project S 11603-N16. Last but not least I want to express my gratitude to *aba.astro.univie.ac.at*, which served as tireless workhorse through many days and nights, performing almost all computations presented in this study.

References

E. Asphaug and W. Benz. Size, Density, and Structure of Comet Shoemaker-Levy 9 Inferred from the Physics of Tidal Breakup. Icarus, 121:225–248, June 1996. doi: 10.1006/icar.1996.0083.

D. Bancelin, E. Pilat-Lohinger, S. Eggl, T. I. Maindl, C. Schäfer, R. Speith, and R. Dvorak. Asteroid flux towards circumprimary habitable zones in binary star systems: I. Statistical Overview. *ArXiv e-prints*, June 2015.

W. Benz and E. Asphaug. Impact simulations with fracture. I - Method and tests. Icarus, 107:98, January 1994. doi: 10.1006/icar.1994.1009.

W. Benz and E. Asphaug. Simulations of brittle solids using smooth particle hydrodynamics. *Computer Physics Communications*, 87:253–265, May 1995. doi: 10.1016/0010-4655(94)00176-3.

W. Benz and E. Asphaug. Catastrophic Disruptions Revisited. Icarus, 142:5–20, November 1999. doi: 10.1006/icar.1999.6204.

S. Diehl, G. Rockefeller, C. L. Fryer, D. Riethmiller, and T. S. Statler. Generating Optimal Initial Conditions for Smooth Particle Hydrodynamics Simulations. *ArXiv e-prints*, November 2012.

R. Dvorak, B. Loibnegger, and T. I. Maindl. On the probability of the collision of a Mars-sized planet with the Earth to form the Moon. *ArXiv e-prints*, June 2015a.

R. Dvorak, T. Maindl, Á. Süli, C. Schäfer, R. Speith, and C. Burger. Collisions of planetesimals and formation of planets. In *Physics of Exoplanets: From Earth-sized to Mini-Neptunes, proceedings of a conference held Feb. 23-27, 2015 at the Kavli Institute for Theoretical Physics/ Edoted by Eric Ford, Louise Kellogg, Geoff Marcy, Burkhard Militzer.*, page 1, February 2015b.

R. Dvorak, T. I. Maindl, C. Burger, C. Schäfer, and R. Speith. Planetary Systems and the Formation of Habitable Planets. *ArXiv e-prints*, February 2015c.

R. A. Gingold and J. J. Monaghan. Smoothed particle hydrodynamics - Theory and application to non-spherical stars. MNRAS, 181:375–389, November 1977.

D. E. Grady and M. E. Kipp. Continuum modelling of explosive fracture in oil shale. *International Journal of Rock Mechanics and Mining Sciences & Geomechanics Abstracts*, 17(3):147–157, 1980. ISSN 0148-9062. doi: {http://dx.doi.org/10.1016/0148-9062(80)91361-3}. URL http://www.sciencedirect.com/science/article/pii/0148906280913613.

Z. M. Leinhardt and S. T. Stewart. Collisions between Gravity-dominated Bodies. I. Outcome Regimes and Scaling Laws. ApJ, 745:79, January 2012. doi: 10.1088/0004-637X/745/1/79.

L. D. Libersky and A. G. Petschek. Smooth particle hydrodynamics with strength of materials. In H. E. Trease, M. F. Fritts, and W. P. Crowley, editors, *Advances in the Free-Lagrange Method Including Contributions on Adaptive Gridding and the Smooth Particle Hydrodynamics Method*, volume 395 of *Lecture Notes in Physics, Berlin Springer Verlag*, pages 248–257, 1991. doi: 10.1007/3-540-54960-9_58.

L. B. Lucy. A numerical approach to the testing of the fission hypothesis. AJ, 82: 1013–1024, December 1977. doi: 10.1086/112164.

T. I. Maindl and R. Dvorak. Collision parameters governing water delivery and water loss in early planetary systems. In M. Booth, B. C. Matthews, and J. R. Graham, editors, *IAU Symposium*, volume 299 of *IAU Symposium*, pages 370–373, January 2013. doi: 10.1017/S1743921313008971.

T. I. Maindl, C. Schäfer, R. Speith, Á. Süli, E. Forgács-Dajka, and R. Dvorak. SPH-based simulation of multi-material asteroid collisions. *Astronomische Nachrichten*, 334:996, November 2013. doi: 10.1002/asna.201311979.

T. I. Maindl, R. Dvorak, C. Schäfer, and R. Speith. Fragmentation of colliding planetesimals with water content. In *IAU Symposium*, volume 310 of *IAU Symposium*, pages 138–141, July 2014. doi: 10.1017/S1743921314008059.

H. J. Melosh. *Impact cratering: A geologic process*. 1989.

H. J. Melosh, E. V. Ryan, and E. Asphaug. Dynamic fragmentation in impacts - Hydrocode simulation of laboratory impacts. J. Geophys. Res., 97:14735, September 1992. doi: 10.1029/92JE01632.

J. J. Monaghan. Smoothed particle hydrodynamics. ARA&A, 30:543–574, 1992. doi: 10.1146/annurev.aa.30.090192.002551.

J. J. Monaghan. Smoothed particle hydrodynamics. *Reports on Progress in Physics*, 68: 1703–1759, August 2005. doi: 10.1088/0034-4885/68/8/R01.

J. J. Monaghan and J. C. Lattanzio. A refined particle method for astrophysical problems. A&A, 149:135–143, August 1985.

A. Morbidelli, J. I. Lunine, D. P. O'Brien, S. N. Raymond, and K. J. Walsh. Building Terrestrial Planets. *Annual Review of Earth and Planetary Sciences*, 40:251–275, May 2012. doi: 10.1146/annurev-earth-042711-105319.

P. Randles and L. D. Libersky. Smoothed Particle Hydrodynamics: Some recent improvements and applications. *Computer Methods in Applied Mechanics and Engineering*, 139:375–408, December 1996. doi: 10.1016/S0045-7825(96)01090-0.

S. T. Riecker. *GPU programming applied to Smoothed particle Hydrodynamics simulations of planetesimal collisions*. Master thesis, Eberhard-Karls-Universität Tübingen, 2014.

C. Schäfer. Application of Smooth Particle Hydrodynamics to selected Aspects of Planet Formation. *Dissertation, Eberhard-Karls Universität, Tübingen, Germany*, 2005.

J. H. Tillotson. Metallic equations of state for hypervelocity impact. Technical Report General Atomic Report GA-3216, General Dynamics, San Diego, CA, 1962.

J. B. Walsh. The Effect of Cracks on the Compressibility of Rocks. J. Geophys. Res., 70:381–389, January 1965. doi: 10.1029/JZ070i002p00381.

W. A. Weibull. *Ingvetensk. Akad. Handl.*, 151:5, 1939.